Oligomerization processes limit photoactivation and recovery of the Orange Carotenoid Protein.

Elena A. Andreeva[1,2], Stanislaw Nizinski[3], Adjélé Wilson[4], Matteo Levantino[5], Elke De Zitter[1], Rory Munro[1], Fernando Muzzopappa[4], Aurélien Thureau[6], Ninon Zala[1], Gotard Burdzinski[3], Michel Sliwa[7], Diana Kirilovsky[4], Giorgio Schirò[1], Jacques-Philippe Colletier[1*].

[1]Institut de Biologie Structurale (IBS), Université Grenoble Alpes, CEA, CNRS, 38044 Grenoble, France

[2] Max-Planck-Institut für medizinische Forschung, Jahnstraße 29, 69120 Heidelberg, Germany

[3]Quantum Electronics Laboratory, Faculty of Physics, Adam Mickiewicz University in Poznan, Uniwersytetu Poznańskiego 2, 61-614 Poznan, Poland

[4]Institute for Integrative Biology of the Cell (I2BC), CEA, CNRS, Université Paris-Sud, Université Paris- Saclay, 91198 Gif-sur-Yvette, France

[5] European Synchrotron Radiation Facility (ESRF), BP 220, 38043 Grenoble, France

[6] Synchrotron Soleil, Beamline SWING, Saint Aubin BP 48, F-91192 Gif Sur Yvette Cedex, France

[7] Univ. Lille, CNRS, UMR 8516, LASIR, LAboratoire de Spectroscopie pour les Interactions, la Réactivité et l'Environnement, Lille 59000, France

[8]Present address: Center for Integrative Biology (CBI), University of Toulouse, CNRS, Toulouse, France

[*]correspondence: colletier@ibs.fr

Abstract (155 words)

The Orange Carotenoid Protein (OCP) is a photoactive protein involved in cyanobacterial photoprotection, by quenching of the excess of light harvested energy. The photoactivation mechanism remains elusive, in part due to absence of data pertaining to the timescales over which structural changes in the protein take place. It also remains unclear whether or not oligomerization of the dark-adapted and light-adapted OCP could play a role in the regulation of its energy quenching activity. Here, we probed photo-induced structural changes in OCP by a combination of static and time-resolved X-ray scattering and steady-state and transient optical spectroscopy in the visible range. Our results suggest that oligomerization partakes in the regulation of OCP photocycle, with different oligomers slowing down the overall thermal recovery of the dark-adapted state of OCP. They furthermore reveal that upon non-photoproductive excitation, a numbed-state forms, which remains in a non-photoexcitable structural state for at least ~0.5 μs after absorption of a first photon.

Significance Statement (120 words):

The orange carotenoid protein (OCP) is a photoactivatable protein involved in cyanobacterial photoprotection. Upon photoactivation, OCP becomes able to quench the excess of energy uptaken by the light-harvesting antennae, thereby evading damage to the cells. It remains unclear, however, what is the exact OCP photoactivation mechanism, and whether or not oligomerization partakes in the regulation of the OCP function. Here, we investigated these two issues by combining static and time-resolved (TR) X-ray scattering and optical spectroscopy. Our results show that OCP oligomerizes both in the dark-adapted inactive and light-adapted active states, suggesting a role for oligomerization. TR scattering data furthermore reveal that the first large-scale conformational changes associated with the photoactivation of OCP take place on the μs time scale.

Introduction (1457 words)

Photosynthetic organisms have evolved to make use of up to 99 % of light harvested energy (1). In most cyanobacteria, the main light harvesting antenna is the phycobilisome (PBS), a soluble complex capable of directly funneling its harvested photon energy into thylakoid-membrane-embedded reaction-centers. In the event of an energy overflow into photosystem II reaction center, charge recombination can occur that will lead to the production of $^1O_2$, which in turn may damage the photosynthetic apparatus (2, 3). The main function of the soluble two-domain photoactive orange carotenoid protein (OCP) is to quench the excessive energy absorbed by the PBS, enabling the dissipation of this energy into heat. This is accompanied by a decrease in the PBS fluorescence. For its energy-quenching function to be elicited, OCP needs to be photoactivated by the absorption of a blue-green photon, which triggers the transition from the dark inactive orange state (OCP^O) to the active red state (OCP^R) (4–11) capable of quenching up to 80 % of the PBS fluorescence (12). As the photoactivation yield of OCP is extremely low (0.2 %) (13) , interactions between PBS and OCP^R only occurs when irradiance threatens cell survival. Additionally, OCP can also quench $^1O_2$, and is thus one of the central players in cyanobacterial photoprotection (14, 15). Phylogenetic investigations have allowed classification of OCP sequences into three clades, viz. OCP1, OCP2 and OCPX (16).

Most research endeavors on OCP (including the present work) have been conducted on the *Synechocystis* PCC 6803 OCP1 variant featuring echinenone (ECN) as the functionalizing carotenoid (17, 18). Nonetheless, the first crystallographic structure of a dark-adapted OCP^O was from the cyanobacteria *Limnospira (Arthrospira) maxima*, and featured 3'-hydroxy-ECN as the natural pigment (14). The structure revealed that OCP folds into two domains separated by a ~20 residue linker (Fig. 1). The N-terminal domain (NTD), comprised of residues 1–165, is the effector domain binding to PBS, while the C-terminal domain (CTD) is comprised of residues 190–317 and serves as the regulator of OCP energy-quenching activity (19). The keto-carotenoid pigment binds in a ~35 Å long hydrophobic tunnel that spans the two domains. The NTD is fully α-helical (αA-αJ), featuring a fold unique to cyanobacteria, whereas the CTD is a seven-stranded β-sheet (β1-β7) sandwiched between two sets of α-helices, viz. αK, αL and αM, on one side (referred to as the F-side), ~~and~~ the terminal αA (residues 1-19; also referred to as the N-terminal extension or NTE) and αN (residues 304-317; also referred to as the the C-terminal tail or CTT), on the opposite side (referred to as the A-side). The two latter have been shown to play important roles in the regulation of OCP photoactivation and recovery. Stabilization of the OCP^O state is achieved at two main interfaces, viz. the NTD/CTD interface, burying 677 $Å^2$ of surface area and featuring two strictly-conserved H-bonds (*i.e.,* R155 to E244, N104 to W277) , and the αA/CTD interface, burying 790 $Å^2$ and featuring six H-bonds (buried surface areas calculated from the *Synechocystis* OCP structure) of which two to the C-terminal αN (L16(O)-A308(N) and A18(N)-L307(O)). Thus, the αA helix is one of the main secondary structure elements to promote the stabilization of the OCP^O structure. Additionally, the carotenoid buries ~990 $Å^2$ of surface area

83 across the two domains (~ 545 and 445 Å^2 in the NTD and the CTD, respectively), establishing two
84 H-bonds with Y201(OH) and W288(Nε1) in the CTD. The pigment is therefore also essential in
85 stabilizing OCP^O.

86 All available crystal structures of OCP^O feature a dimer, wherein monomers are associated through
87 contacts between facing αA, αB and αH helices, burying ~1090 Å^2 at the dimerization interface. Due
88 to the high concentration of OCP^O within crystals (20-30 mM, depending on the crystal structure
89 considered), the prevalence of OCP^O in its dimeric form was, until recently, regarded as a
90 crystallization artifact and therefore overlooked (17). Recent results obtained using native mass
91 spectrometry have since shown that OCP^O dimers can form in solution at concentrations as low as 3
92 μM (0.1 mg/ml) (20). The presence of OCP^O dimers was also observed by size exclusion
93 chromatography (SEC) and in small-angle X-ray/neutron scattering (SAXS/SANS) experiments (21,
94 22), which furthermore identified the crystallographic dimer as that which naturally occurs. Additionally
95 supporting the hypothesis that OCP^O dimers could form *in vivo* is the report that the mutation of a
96 single (R27) of the three highly-conserved residues (D19, R27, S134) among the 22 making up the
97 dimerization interface (17) results in a constitutively monomeric mutant (10). Further adding to this
98 complexity is the question as to whether or not OCP^R can also oligomerize, which has been supported
99 by recent SAXS/SANS data (21, 22) but not by native mass spectrometry (10, 20, 23, 24). Altogether
100 these results raise cogent questions as to if and how oligomerization participates in the regulation of
101 OCP function.

102 The exact photoactivation mechanism of OCP – meaning, accumulation of OCP^R, not the mere
103 appearance of a red spectrum – remains elusive. Indeed, despite the use of different experimental
104 approaches to probe the OCP^O to OCP^R transition with a high resolution in either time (25–27) or
105 space (18, 28–30), uncertainties remain regarding the exact sequence of events leading to
106 photoactivation – in part due to the absence of a high resolution structure of metastable OCP^R and
107 because a consensus remains to emerge regarding the events occurring on the ultra-fast timescales
108 (15, 25), but also because data pertaining to the (long) timescales over which (large-scale) structural
109 changes take place are lacking. All investigators agree on the fact that upon photon absorption, the
110 carotenoid pigment transitions to an excited S_2 state, which decays within ~0.1 ps into multiple ps-
111 lived excited states (S_1, ICT, S*). Only one of these presumably leads to the minute-lived OCP^R state
112 after the formation of at least three different intermediates (photoproducts P_1, P_2, P_3) over the ps-μs
113 timescale (25). Thus, the formation of OCP^R is mainly limited by picosecond (ps) timescale excited
114 state dynamics, with ~ 99 % of carotenoids relaxing back to the ground state along non-productive
115 pathways. It was suggested that photoproduct P_1 is characterized by rupture of the H-bonds between
116 the carotenoid and the protein; P_2 by a repositioning of the β1-ring in the CTD, putting its carbonyl
117 oxygen at a distance incompatible with H-bonding to Tyr201(OH) and W288(Nε1); and P_3 by the

118 translocation (12 Å) of the carotenoid into the NTD. The dissociation of helix αA and αN from the A-
119 side of the CTD was suggested to await the millisecond (ms) time scale (24), and to be followed by
120 dissociation of the two domains yielding OCP^R. This hypothesis has since been supported by SEC
121 and SAXS (28). By specific labeling of accessible carboxylate groups, mass spectrometry further
122 pointed to a signal transduction mechanism whereby, upon photoactivation and rupture of H-bonds
123 between the carotenoid and the CTD, disorder is propagated across the CTD β-sheet resulting in a
124 detachment of the N-terminal helix αA and subsequent dissociation of the dimer through
125 destabilization of helix αB. Direct structural evidence for the existence of these steps is yet still lacking.
126 Most recently, experiments carried out on an OCP mutant wherein H-bonding of the carotenoid to the
127 CTD is modified supported the existence of two additional intermediate states between P_3 and OCP^R,
128 namely P_M and P_X, proposed to be characterized by dissociation of the αA and αN helices,
129 respectively (27). It yet remains unclear whether these states also exist in the wild-type (wt) protein.

130 In the present work, we used a combination of mutagenesis, transient spectroscopy in visible range,
131 and static and time-resolved X-ray solution scattering to clarify (i) the oligomerization states of OCP^O
132 and OCP^R in solution, (ii) the timescale over which large-scale structural changes take place during
133 photoactivation, and (iii) whether or not pulsed-illumination permits the formation of OCP^R. By
134 conducting static SAXS experiments on the wt OCP and on a stable monomeric R27L mutant (10),
135 wherein the conserved R27-D19 salt-bridge at the dimerization interface is suppressed, we obtained
136 confirmation that both OCP^O and OCP^R can oligomerize in solution, suggesting a role for
137 oligomerization in the regulation of OCP activity. Using TR-SAXS, we obtained evidence that the 'red'-
138 shifted state generated by pulsed illumination, which forms and decays within ~10 μs and ~10-200
139 ms (depending on the his-tag location), respectively, differs from the OCP^R state accumulated under
140 stationary illumination conditions, which forms and decays within ~1 ms and ~1-30 min (depending
141 on concentration), respectively. Our data furthermore reveal that upon a non-productive pulsed
142 photoexcitation – *i.e.* in the 99.7 % of the cases where OCP^R does not form – OCP remains in a non-
143 photoexcitable structural state for at least ~ 0.5 μs, despite the carotenoid returning back to the
144 electronic ground state within tens of ps and the protein featuring a spectrum characteristic of the
145 OCP^O state (25).

146

147

148

Materials and Methods (2499 words)

Protein expression and sample preparation.

OCP expression and extraction were carried out as described in Gwizdala et al. (8) and Bourcier de Carbon et al. (31). Briefly, expression in the holo form of the N-terminally his-tagged *wild-type* OCP ($OCP_{wt\text{-}Ntag}$) and the N-terminally his-tagged monomeric mutant ($OCP_{R27L\text{-}Ntag}$) was achieved by respective transformation of the *pCDF-NtagOCPSyn* or *pCDF-NtagOCPSynR27L* plasmids into ECN-producing BL21 (DE3) *E.coli* cells – *i.e.* cells previously transformed with the pAC-BETA and pBAD-CrtO plasmids described in Bourcier de Carbon et al. (31). Expression in *Synechocystis* cells of the holo form of C-terminally his-tagged *wild-type* OCP ($OCP_{wt\text{-}Ctag}$) was achieved using the protocol described in Gwizdala et al. (8). The proteins were purified in three steps including affinity chromatography on a Ni-NTA column (Ni-Probond resin, Invitrogen), hydrophobic chromatography on a phenyl-sepharose column (HiTrap Phenyl HP, GE Healthcare) and size exclusion chromatography on an analytical HiLoad 16/60 Superdex 75 (HiLoad 16/600 Superdex 75 pg, Sigma Aldrich). Proteins were eluted from the latter at a flow rate of 1 ml/min using a buffer composed of 50 mM Tris-HCl pH 7,4 and 150 mM NaCl. To assert the molecular weight of eluted species, the column was previously calibrated using the following standard proteins: γ-globulin (158 kDa), ovalbumin (44 kDa), myoglobin (17 kDa) and vitamin B12 (1.35 kDa). OCP concentrations were estimated from the absorbance signal at 490 nm, using the extinction coefficient of 63000 M^{-1} cm^{-1} ~~recently~~ proposed by Sluchanko et al. (32). We note that an uncertainty remains as to the exact extinction coefficient that should be used to derive OCP concentration from absorbance measurement. Protein concentration is nowadays generally estimated using the absorbance signal at 280 nm and a calculated extinction coefficient (e.g. obtained from https://web.expasy.org/cgi-bin/protparam/protparam (33, 34)), which in the case of *Synechocystis* OCP amounts 34 659 $M^{-1}.cm^{-1}$. This value agrees well with the extinction coefficient at 490 nm proposed by Sluchanko et al., as the ratio between the 490 and 280 nm peaks is ~2 for the pure protein, but it neglects the potential absorption of the ketocarotenoid pigment at 280 nm. Thus far, most of the papers published on OCP have accordingly used an extinction coefficient of 110 000 M^{-1} cm^{-1} at 490 nm, based on the debatable assumption that the ketocarotenoid pigment has similar absorption spectrum when bound to OCP or dissolved in organic solvents. Indeed, if there is no absorbance of the carotenoid at 280 nm, then one expects a ratio of ~3 between the absorbances peak at 490 nm and 280 nm. But if we consider absorption of the carotenoid at 280 nm, and assume the same extinction coefficient in the protein cage as in organic solvents – *i.e.* roughly 15 % of the absorption peak at 490 nm (measured by us as well as others) – then the measured ratio of ~2 between the absorbance at 490 and 280 nm can be rationalized since $A_{280\ nm}$ = (0.33+0.15) *$A_{490\ nm}$ = 0.48* $A_{490\ nm}$. At present, we cannot favor either hypothesis. However, as our current aim is to report on oligomerization processes, we believe it is preferable that we underestimate – rather than overestimate – dissociation constants. Hence, the concentrations reported in the present paper were estimated using the conservative extinction coefficient of 63 000 M^{-1} cm^{-1} (32). The actual

concentrations and dissociation constants could yet be 1.7 times lower if the ketocarotenoid absorbs at 280 nm and the real extinction coefficient of OCP at 490 nm is 110 000 $M^{-1}.cm^{-1}$.

Static SAXS measurements.

Static X-ray scattering data were collected at 21°C on an EigerX-4M detector at the SWING beamline of the Soleil Synchrotron (Saint-Aubin, France). X-ray solution scattering patterns in the SAXS region (q = 0.02 - 0.5 $Å^{-1}$) were collected for $OCP_{wt\text{-}Ctag}$ and $OCP_{R27L\text{-}Ntag}$ at various concentrations using a polychromatic X-ray beam centered at 16 keV and an EigerX-4M (Dectris) detector. Two sets of measurements were carried out, before and after 30 min irradiation of OCP solutions with a 430 nm LED source (~ 500 mW/cm²), allowing collection of X-ray scattering signals in the dark-adapted (OCP^O) and light adapted (OCP^R) states, respectively. For $OCP_{wt\text{-}Ctag}$, data were acquired at 0.7, 3.5, 10.5 and 23 mg/ml for the OCP^O and 0.7, 3.5 and 10.5 mg/ml for the OCP^R state, while for $OCP_{R27L\text{-}Ntag}$, data were recorded at 0.7, 3.5, 10.5 and 14 mg/ml for the OCP^O state and at 0.7, 3.5 and 10.5 mg/ml for the OCP^R state. For each concentration, 30 X-ray scattering patterns (each registered after 990 ms of X-ray exposure) were collected with 30 analogous patterns of the buffer before and after each protein measurement. Each 2D pattern was converted to a 1D scattering pattern by azimuthal integration using the Foxtrot-3.5.2 software available at the SWING beamline. Corresponding scattering patterns were averaged and protein signals were obtained by subtraction of buffer scattering. The distance distribution functions were computed using GNOM (35) and the parameters reported in Table S1 were determined from the reduced data using relevant programs from the ATSAS suite (35, 36). Low-resolution molecular envelopes were computed using the ATSAS reconstitution tool DAMMIF (37, 38). To construct the OCP^R dimer and tetramer models, we used the published structures of paralogs of the isolated N-terminal and C-terminal OCP domains, viz. the crystal structures of *Anabaena Nostoc* PCC 7120 and *Fremyella diplosiphon* HCP (pdb ids: 6MCJ and 5FCX, respectively) (39, 40) and of *Anabaena Nostoc* PCC 7120 CTDH (pdb id: 5FEJ) (41), respectively. Our modeling strategy is presented in the Results section.

Spectroscopic monitoring of the OCP^R to OCP^O thermal recovery after accumulation of OCP^R by a prolonged continuous illumination.

Thermal recovery was investigated as a function of concentration on the three OCP variants, using a JASCO V-630 UV/Vis spectrophotometer (Easton, USA). Purified proteins in $OCP_{R27L\text{-}Ntag}$ and $OCP_{wt\text{-}Ctag}$ were assayed at 0.1, 1.7, 3 and 16 mg/ml, and $OCP_{wt\text{-}Ntag}$ at 0.1, 3, 10 and 16 mg/ml. Specifically, the absorption at 467 nm was monitored at room-temperature (21 °C) in the dark following 30 minutes of continuous blue light irradiation with a 430 nm LED light collimated to 1 cm (~ 500 mW/cm²) to maximize accumulation of OCP^R and reproduce the conditions used in the static SAXS experiments. Measurements at 0.1 mg/ml were carried out in a PMMA cuvette with 1 cm

pathlength, those at 1.7, 3 and 10 mg/ml in a quartz cuvette with 0.1 cm pathlength, and that at 16 mg/ml in an Infrasil cuvette with 0.05 cm pathlength.

To facilitate comparison of data collected at various concentrations, the absorption difference at 467 nm was normalized using $A_{Norm} = [A(t) - A(t_0)]/[A(t_{max}) - A(t_0)]$, where $A(t)$, $A(t_0)$ and $A(t_{max})$ are the absorption values measured at a generic time t after switching off the 430 nm light; at time t_0 (*i.e.,* just after illumination at 430 nm was switched off, when the concentration of OCP^O is at its minimum); and at the time t_{max} when the starting OCP^O state has recovered, respectively. The non-linear least-squares optimization and parameter extraction were performed using LMFIT (42). After individual fits of each curve data pointed to the necessity to use at least three exponential components to fit the recovery data, we opted for a per-OCP variant global-fitting of the normalized absorption data. For each sample, the recovery data measured at four concentrations were jointly fitted using either a triple or a quadruple exponential function,

$$A(t) = a_{ci-1} \times \left[1 - exp\left(\frac{-t}{\tau_{ci-1}}\right)\right] + a_{ci-2} \times \left[1 - exp\left(\frac{-t}{\tau_{ci-2}}\right)\right] + a_{ci-3} \times \left[1 - exp\left(\frac{-t}{\tau_{ci-3}}\right)\right] + a_{ci-4} \times \left[1 - exp\left(\frac{-t}{\tau_{ci-4}}\right)\right]$$

where a_{ci-1}, a_{ci-2}, a_{ci-3} and a_{ci-4} are concentration-dependent pre-exponential factors, τ_{ci-1}, τ_{ci-2}, τ_{ci-3} and τ_{ci-4} are process-dependent characteristic times, and a_{ci-4} is fixed to zero in the case of a triple exponential fit. A better fit was obtained with four exponential componentsfor the $OCP_{wt\text{-}Ctag}$ recovery data, but improvements were marginal for the data collected on $OCP_{wt\text{-}Ctag}$ and $OCP_{R27L\text{-}Ntag}$, with amplitudes for the fourth component consistently inferior to 0.1 (see Table S2 and Table S3). Hence, we retained results from the four exponential fit for $OCP_{wt\text{-}Ctag}$, but from the three exponential fit, for the two N-tagged variants. We nonetheless present results for both types of fits in Fig. 3, Supplementary Fig. S5 and S6, and Tables S2 and S3.

Spectroscopic monitoring of the spectral evolution after ns-pulsed excitation at 470 nm.
Measurements were performed using the custom apparatus described previously (43). OCP^O photo-excitation was achieved using a 470 nm nanosecond laser delivering 5 mJ energy per 8 ns pulse at a repetition rate of 0.05 Hz. The probing beam was filtered using a bandpass filter, so that only 440 nm (FWHM: 9 nm) or 565 nm (FWHM: 12 nm) light passed through the sample, avoiding putative probe-induced effects from the white spectrum of the xenon lamp. Scattered pump light was reduced by a notch filter set installed upstream of the monochromator which precedes the photomultiplier tube. All measurements were carried out at a sample absorbance of ~ 0.7 at 470 nm. For the lowest concentration, a 10 x 10 mm cuvette was used, which was set with a right-angle configuration between the pump and the probe beams. For higher concentrations, 2 mm and 500 µm flat cuvettes were used,

252 affording to increase the concentration whilst keeping the absorbance in the optimal range. Use of
253 these cuvettes required a quasi-collinear (≈ 5° angle) configuration between the pump and probe
254 beams. Measurements were performed at different temperatures ranging from 8 to 36° C. Stirring
255 was not applied to avoid sample displacement from the probed volume at longer time delays. All
256 experiments were repeated 100 times on each of 4 partially-overlapped time-windows, altogether
257 covering the 50 ns - 1 s time-range. Recorded data were merged and projected on a logarithmic grid.
258 Stability of the protein was checked by its steady-state absorbance after each experiment. The
259 quantum yield formation of photo-products was determined using ruthenium as actinometer (32, 44)
260 and molar absorption coefficient of OCP^O at 490 nm = 63000 $cm^{-1}.M^{-1}$ (32).

261 **Time-resolved X-ray scattering.**

262 Time-resolved WAXS experiments were performed at the ID09 beamline (European Synchrotron
263 Radiation Facility (ESRF), Grenoble, France) (45). X-ray solution scattering patterns in the WAXS
264 region (q = 0.01 – 2.5 $Å^{-1}$) were collected at 23 mg/ml (620 μM) for $OCP_{wt\text{-}Ntag}$ and $OCP_{wt\text{-}Ctag}$ using a
265 polychromatic X-ray beam centered at 15 keV and a Rayonix MX170-HS detector placed 350 mm
266 from the sample. The protein samples, $OCP_{wt\text{-}Ntag}$ and $OCP_{wt\text{-}Ctag}$, were photoactivated with circularly-
267 polarized laser pulses from two different laser systems: either an EKSPLA NT342B laser or a
268 COHERENT Evolution laser. While the first laser is a tunable laser generating laser pulses with a
269 duration of 5 ns (full width half maximum, FWHM) at a maximum repetition rate of 10 Hz, the second
270 laser runs at 1 kHz, has a fixed wavelength (527 nm) and has a pulse duration that can be modulated
271 by changing the current of its diode pump. The use of the COHERENT Evolution laser allowed us to
272 perform a set of experiments with pulse durations longer than those of the EKSPLA laser (in particular,
273 experiments with 300 or 450 ns long pulses were performed); moreover, it allowed us to excite the
274 protein sample with either a single laser pulse or a burst of several laser pulses (up to 30) at 1 kHz.
275 For each experiment, the required number of photoexcitation laser pulses were extracted from the
276 train of pulses generated by the Evolution laser by means of a pair of synchronized fast mechanical
277 shutters (Lambda SC, Sutter). By changing the relative delay of the first shutter opening and of the
278 last shutter closing, it was possible to cleanly select either a single laser pulse or several. In all
279 experiments, the laser beam was focused with cylindrical lenses to an elliptical spot approximately
280 2.5 × 0.25 mm^2 (FWHM) and the energy was regulated so as to have an energy density of ~ 3 mJ/mm^2
281 at the sample position, corresponding to ~ 75 absorbed photons per chromophore.

282 To maximize the overlap between the pump- and probe-illuminated volumes, an orthogonal pump–
283 probe geometry was employed, with the X-ray beam (0.06 × 0.1 mm^2, FWHM) hitting the sample
284 capillary 0.3 mm from its edge. In order to both minimize X-ray radiation damage and allow the
285 recovery of the OCP^O state, the protein solution (~ 5 ml) was circulated with a peristaltic pump (Gilson
286 Minipuls 3) through a 2 mm X-ray quartz capillary in a closed loop. During the flow, most of the sample

287 was contained in a small reservoir kept in the experimental hutch, thermalized at 22 °C. The flow
288 speed was set according to both the optical-laser pump – X-ray probe time delay and the repetition
289 rate, allowing the sample to be kept in the pump–probe intersection area during a pump–probe
290 sequence while refreshing it between two consecutive pump pulses. Single X-ray pulses were
291 selected from the synchrotron pulse train by means of a high-speed chopper and a millisecond
292 shutter. Up to 30 scattering patterns per time delay were acquired and averaged to improve the signal-
293 to-noise ratio. Laser-off (dark) images were also acquired with the X-ray pulse arriving 50 ms before
294 the laser pulse and used as a reference to compute the difference patterns after normalization to the
295 water peak (2 - 2.2 $Å^{-1}$) (46). Difference patterns were azimuthally averaged and the peak of the
296 undulator spectrum (~ 0.83 $Å^{-1}$) was used as the reference to convert the scattering angle to the
297 momentum transfer q. Independent TR-WAXS measurements on a solution of 4-amino-1,1′-
298 azobenzene-3,4′-disulfonic acid monosodium salt with an optical density comparable to the OCP
299 sample were used to correct the water heating scattering signal of the collected OCP data (46). TR-
300 WAXS was also used to follow the OCP^R to OCP^O thermal recovery with a direct structurally sensitive
301 technique. In particular, X-ray scattering patterns were collected over 30 minutes from a sample of
302 $OCP_{wt\text{-}Ctag}$ that had been exposed for 30 minutes to continuous illumination by a 430 nm LED light.

303 The TR-X-ray scattering dataset was further analyzed by a singular value decomposition (SVD)
304 analysis using a custom-written Python script. The time-dependent difference patterns form a j × k
305 matrix, with j the number of q values and k the number of time delays. The SVD algorithm calculates
306 the matrices U and V and the vector S, so that $A = U \times S \times V^T$. The columns of matrix U are called left
307 singular vectors, or basis patterns, the rows of V^T are called right singular vectors, or amplitude
308 vectors, and the elements of S are called singular values. The basis patterns are ordered following
309 the high-to-low sorting of singular values. The SVD analysis of kinetic data provides a subset of time-
310 independent patterns containing the relevant information out of the random noise. The dataset can
311 be then reproduced as a linear combination of such time-independent patterns. Inspection of the
312 shape of basis patterns, amplitude vectors and singular values together with the autocorrelation
313 analysis of both basis patterns and amplitude vectors (47) indicates that only one component contains
314 significant information. Hence, a two-step model (with growing and decaying exponentials) was used
315 to fit the evolution of the integrated time-resolved X-ray scattering signal.

316

317 **Results (5901 words)**

318

319 **Soluble OCP^O can form dimers in solution.**

320 We used small-angle X-ray scattering to investigate the oligomerization state of dark-adapted OCP
321 (OCP^O) in solution. For this purpose, we worked on two proteins: (i) a wt OCP, functionalized by ECN
322 and featuring a six-histidine tag (6Xhis-tag) at the C-terminus ($OCP_{wt\text{-}Ctag}$); and (ii) a R27L monomeric
323 mutant, functionalized by ECN and featuring a 6Xhis-tag at the N-terminus ($OCP_{R27L\text{-}Ntag}$). Use of the
324 latter, wherein the conserved D19 – R27 salt bridge is suppressed, afforded a control for the X-ray
325 scattering signal of an OCP monomer (10).

326 Data were first collected on dark-adapted $OCP_{wt\text{-}Ctag}$ and $OCP_{R27L\text{-}Ntag}$ at increasing protein
327 concentrations, informing on the OCP^O state. The buffer-subtracted scattering patterns of dark-
328 adapted $OCP_{wt\text{-}Ctag}$ and $OCP_{R27L\text{-}Ntag}$ are shown in Fig. 2*A* and 2*B*. For $OCP_{R27L\text{-}Ntag}$ at all
329 concentrations, the radii of gyration (Rg) derived from the Guinier region are similar (Fig. 3*A*), and the
330 derived pairwise distance distribution functions P(r) overlay (Fig. 2*C*). Accordingly, the low-resolution
331 molecular envelopes calculated by the DAMMIF algorithm (48) from the dark-adapted $OCP_{R27L\text{-}Ntag}$
332 data collected at 0.7, 3.5, 10.5 (Fig. 4) and 14 mg/ml (Fig. S1) are comparable, both matching the
333 crystallographic OCP^O monomer. Hence, the $OCP^O{}_{R27L\text{-}Ntag}$ sample remains in the same monomeric
334 state at all tested concentrations and is therefore a good control for monomeric OCP^O. Contrastingly,
335 examination of the P(r) for dark-adapted $OCP_{wt\text{-}Ctag}$ samples (Fig. 2*C*) reveals an increase in pairwise
336 distances when the concentration exceeds 3.5 mg/ml and, accordingly, an increase is observed in
337 the radii of gyration derived from the Guinier region (Fig. 3*A*). These two observations indicate that
338 the average size of dark-adapted $OCP_{wt\text{-}Ctag}$ increases with concentration. The low-resolution
339 molecular envelopes calculated by DAMMIF (37) from the dark-adapted $OCP_{wt\text{-}Ctag}$ data are consistent
340 with the presence of a predominant OCP^O dimer (Fig. 4 and Fig. S1) at concentrations $\gtrsim$ 3.5 mg/ml,
341 and a mixture of monomers and dimers at 0.7 mg/ml. It is of important note that the above
342 assignments of molecular envelopes to monomers and dimers agree with the molecular weight
343 estimates from I(0) (49) (see Table S1 (*i.e.*, the intensity extrapolated at q=0)) after scaling data on
344 absolute units.

345 We used the program OLIGOMER (38) to estimate the relative abundance of monomers and dimers
346 in the dark-adapted $OCP_{wt\text{-}Ctag}$ samples prepared at different concentrations (Fig. 3*B*). Calculated X-
347 ray scattering curves for dimeric and monomeric OCP^O were generated from the crystal structure of
348 *Synechocystis* PCC 6803 OCP (pdb id: 3MG1) (17) (Fig. 1) and used for deconvolution of the
349 experimental scattering patterns measured at increasing concentrations (see Materials and Methods).
350 The fit suggests that at 0.7 mg/ml (~ 20 μM), dark-adapted $OCP_{wt\text{-}Ctag}$ is present as a 1:1 mixture of

351 monomers and dimers. The latter attain dominance at ~3.5 mg/ml (~ 100 μM) with a dissociation
352 constant of around 0.5 mg/ml (~ 14 μM).

353 **Illumination induces a dissociation of the dark OCP^O dimer and the formation of OCP^R dimers**
354 **and tetramers.**
355 To provide details on the large-scale conformational changes accompanying the $OCP^O \rightarrow OCP^R$
356 transition, including possible change(s) in oligomeric state, we also collected X-ray scattering data on
357 light-adapted $OCP_{wt\text{-}Ctag}$ and $OCP_{R27LNtag}$ at 0.7, 3.5 and 10.5 mg/ml (Fig. 2*D* and 2*E*). To assess the
358 time required for the accumulation of photoactive $OCPwt_{\text{-}Ctag}$ and $OCP_{R27L\text{-}Ntag}$ states, we carried out
359 preliminary pre-illumination experiments at ESRF-ID09. A highly-concentrated protein solution (30
360 mg/ml) of $OCP_{wt\text{-}Ctag}$ was used, which was presented to the X-ray beam in a 2 mm thick glass capillary.
361 Firstly, a reference pattern was collected on the dark-adapted protein, after which the protein was
362 illuminated by exposure to a 430 nm LED. The distance between the light source and the sample was
363 such that the diameter of the illumination spot was ~ 1 cm at sample position. Scattering patterns
364 were collected every 15 s, each with 750 ms X-ray exposure, and two illumination powers were
365 consecutively tested, viz. 250 and 500 mW. Only after tens of minutes of illumination at 500 mW was
366 accumulation of OCP^R found to reach a plateau, in our experimental conditions (Fig. S2). Therefore,
367 all subsequent experiments aimed at characterizing the active OCP^R state involved ~ 30 minutes
368 illumination by the 500 mW continuous LED source emitting at 430 nm prior to data collection.

369 A concentration series was recorded for $OCP_{R27LNtag}$ and $OCP_{wt\text{-}Ctag}$, each in their light adapted state,
370 at the SWING bio-SAXS beamline (Synchrotron SOLEIL). Absolute X-ray scattering patterns for
371 $OCP^R_{wt\text{-}Ctag}$ and $OCP^R_{R27L\text{-}Ntag}$ are shown in Fig. 2*D* and 2*E*, strongly differing from those obtained, at
372 the same concentrations, for the corresponding proteins in their dark state. The patterns exhibit a
373 dependence on protein concentration, with the low-resolution signal increasing as the latter
374 augments. The derived Rg accordingly increases with concentration, being 32.5 and 29 Å for
375 $OCP^R_{R27L\text{-}Ntag}$ and $OCP^R_{wt\text{-}Ctag}$ at 0.7 mg/ml, 34 Å for both $OCP^R_{R27L\text{-}Ntag}$ and $OCP^R_{wt\text{-}Ctag}$ at 3.5 mg/ml,
376 and 44.9 and 43.8 Å for $OCP^R_{R27L\text{-}Ntag}$ and $OCP^R_{wt\text{-}Ctag}$ at 10.5 mg/ml, respectively (Fig. 3*A* and Table
377 S1). These values are far larger than those observed for the dark-adapted counterparts, but notably
378 similar for the two proteins at each of the three tested concentrations (0.7, 3.5 mg/ml and 10.5 mg/ml).
379 The increase in the size of $OCP_{R27L\text{-}Ntag}$ and $OCP_{wt\text{-}Ctag}$ upon illumination, the dependence of this size
380 to concentration, and the similarity between $OCP^R_{R27L\text{-}Ntag}$ and $OCP^R_{wt\text{-}Ctag}$ at comparable
381 concentrations can also be deduced from the derived P(r) (Fig. 2*F*) and from the MW derived from
382 I(0) estimation (49) (Table S1). Thus, our results not only indicate an overall expansion of the protein
383 upon illumination, but also a change in the OCP^R quaternary structure as a function of concentration.
384 Similar results (notwithstanding a missing data point for 2 mg/ml concentration) were obtained with
385 $OCP^R_{wt\text{-}Ntag}$ (not shown). For each protein, a light minus dark difference scattering pattern $\Delta S(q)$ was

386 calculated at the highest tested concentration (10.5 mg/ml), offering a signature of the change in
387 scattering signal upon illumination (Fig. 3*C*). The $\Delta S(q)$ for $OCP_{wt\text{-}Ctag}$ is characterized by the presence
388 of a negative peak at ~ 0.05 $Å^{-1}$ and a positive peak at ~ 0.12 $Å^{-1}$, whereas for $OCP_{R27L\text{-}Ntag}$, a negative
389 peak is observed at ~ 0.07 $Å^{-1}$ and a positive peak at ~ 0.14 $Å^{-1}$ (Fig. 3*C*). Since $OCP^{R}_{R27L\text{-}Ntag}$ and
390 $OCP^{R}_{wt\text{-}Ctag}$ adopt similar states at 10.5 mg/ml, the displacement of negative and positive peaks
391 presumably emanates solely from the difference between dark-adapted structures, viz. $OCP^{O}_{R27L\text{-}Ntag}$
392 and $OCP^{O}_{wt\text{-}Ctag}$.

393 We used DAMMIF to compute the low-resolution molecular envelopes of $OCP^{R}_{R27L\text{-}Ntag}$ and $OCP^{R}_{wt\text{-}}$
394 $_{Ctag}$ at the three tested concentrations (0.7, 3.5 mg/ml and 10.5 mg/ml). At 0.7 and 3.5 mg/ml (20 and
395 100 µM), we obtained for both $OCP_{wt\text{-}Ctag}$ and $OCP_{R27L\text{-}Ntag}$ an envelope consistent with the presence
396 of a dimer formed by two elongated OCP molecules wherein the NTD and CTD are separated (Fig.
397 4). While at odd with the report of Gupta et al. (28), these results agree with the findings of Golub et
398 al. (21) who earlier reported a similar structure for $OCP^{R}_{wt\text{-}Ctag}$ at 1 and 65 mg/ml (*i.e.* 28 µM and 1.8
399 mM) based on SAXS and SANS data. The molecular envelopes computed for $OCP^{R}_{R27L\text{-}Ntag}$ and
400 $OCP^{R}_{wt\text{-}Ctag}$ at 10.5 mg/ml (300 µM), however, are both consistent with the presence of up to four
401 elongated OCP molecules, suggesting that oligomers of higher-order than dimers can form at
402 increased concentrations – presumably, OCP^{R} tetramers (Fig. 4). Again, the assignment of these
403 molecular envelopes to tetramers is supported by the molecular weights derived from I(0). Differences
404 between our findings and those of Golub et al. (21) could arise from the difference in ionic strength of
405 buffer solutions, as these investigators used 10 mM phosphate buffer at pH 7.4 whereas here, we
406 used 50 mM Tris-HCl pH 7.4 complemented with 150 mM NaCl. Presence of NaCl was intended to
407 reproduce the osmolarity of cyanobacterial cells and could have favored the formation of tetramers.

408 We attempted to model the OCP^{R} structures assuming that : i) OCP^{R} dimers and tetramers are
409 related, *i.e.* tetramers form from the coalescence of two OCP^{R} dimers; ii) interactions between OCP^{R}
410 monomers in a dimer and between OCP^{R} dimers in a tetramer should be symmetrical, *i.e.* they should
411 involve the same interface in the two interacting proteins; iii) functional OCP^{R} dimers should assemble
412 via their CTD so that their two NTD are exposed and free to interact with PBS via R155 (50);
413 consequently, OCP^{R} tetramers would form from an interaction between two NTD in the OCP^{R} dimer,
414 yielding a larger entity with as many exposed – per say functional – NTD moieties as the OCP^{R} dimer;
415 iv) the interfaces allowing the assembly of OCP^{R} dimers and tetramers should not involve R27 (and
416 by extension, the dark dimerization interface contributed by helix αB) since the R27L mutant – unable
417 to form OCP^{O} dimers – is capable of forming OCP^{R} dimers and tetramers; v) rather the CTD-CTD and
418 NTD-NTD interfaces involved in OCP^{R} oligomerization should feature residues that are not exposed
419 in the dark OCP^{O} dimer, nor present at symmetrical crystal contacts in the OCP^{O} structure, otherwise
420 OCP^{O} tetramers and higher oligomers would form in the dark-adapted state; presumably, these would

421 be residues present at the NTD-CTD interface in the dark OCP^O – an assumption which echoes the
422 earlier proposal of Moldenhauer et al. 2017 (51) and Muzzopappa et al. (10, 51, 52) that the interface
423 between CTD domains in an OCP^R dimer should overlap with the CTD surface that interacts with the
424 NTD in OCP^O; vi) the interfaces allowing the assembly of OCP^R dimers and tetramers may already
425 have been observed in available crystal structures of OCP and isolated OCP domains, e.g. in the
426 structure of the isolated holo-NTD of *wt* OCP (18), or in those of NTD and CTD paralogs, respectively
427 coined helical carotenoid proteins (HCP) and CTD-homologues (CTDH) in the literature (39–41).
428 Indeed, the study of Harris et al. (41) has shown that the apo-*Anabaena* CTDH – a homologue of the
429 CTD of OCP involved in carotenoid transport and wherein the C-terminal helix is not apposed onto
430 the β-sheet – is capable of forming two types of dimers, associating either through back-to-back (A-
431 type) or head-to-head (F-type) interactions between two CTDHs. The F-type dimer, wherein CTDH
432 residues equivalent to those contributing to carotenoid binding in the CTD of OCP^O face one another
433 reconstituting a carotenoid tunnel, was proposed to be involved in carotenoid uptake (41). In absence
434 of the carotenoid, however, the A-type interface can form between CTDH molecules, and it was
435 demonstrated by SAXS that the isolated apo-CTD of OCP^O dimerizes by this interface. Golub et al.
436 accordingly proposed that the two OCP^R monomers in a dimer also interact by this interface (10, 22).
437 Like them, we hypothesize that OCP^R dimers form through interaction at this interface, which fulfills
438 our above requirements for a sound modeling of OCP^R oligomers. It was further verified that only the
439 A-type interface can fit the extended molecular envelope derived from our data. Indeed, the F-type
440 interface would result in a "Z"-shaped molecular envelope. In the dark OCP^O, interaction by the A-
441 interface is prevented by the presence of helices αN (CTT, corresponding to residues 304-317) and
442 αA (or NTE, corresponding to residues 1-17) which appose aside on the external face of the β-sheet
443 but detach upon photoactivation. These helices were therefore considered as disordered in OCP^R
444 and not included in our OCP^R dimer model. To avoid clashes, and account for the known exposure,
445 in OCP^R, of the face of the NTD that interacts with the CTD in OCP^O – and notably R155, which is
446 required for the interaction of OCP^R with PBS, and stabilizes the NTD/CTD interface of OCP^O by
447 hydrogen bonding to E244 – the NTD was rotated by 180° and translated by 10 Å. The OCP^R dimer
448 was then used as a starting point for modeling the tetramer, by assembly of two NTD in a fashion
449 reminiscent to that observed in the HCP crystal structures from *Anabaena* Nostoc PCC 7120 and
450 *Fremyella diplosiphon* (pdb ids: 5FCX and 6MCJ, respectively) (39, 40). In these, two molecules are
451 found in the asymmetric unit, forming a dimer assembled through a symmetrical interface, featuring
452 at its center the residue equivalent to R155 in OCP. Hence, in our model, the two dimers in an OCP^R
453 tetramer interact by the same face known to bind the PBS, leaving two NTD available for binding to
454 the latter. This tetramer model fits the *ab initio* envelopes computed for $OCP^R_{R27L\text{-}Ntag}$ and $OCP^R_{wt\text{-}Ctag}$
455 at 10.5 mg/ml (300 μM) (Fig. 4).

456

457 **Kinetics of OCP^R → OCP^O thermal recovery after accumulation of OCP^R by continuous**
458 **illumination.**
459 The recoveries of the OCP scaffold and the carotenoid structure could be uncoupled. Hence, with aim
460 to split a difference between the structural recovery (informing on the protein structure) and the
461 spectral recovery (informing on the electronic structure and environment of the carotenoid pigment),
462 we monitored the kinetics of thermal OCP^R to OCP^O recovery using SAXS ($OCP_{wt\text{-}Ctag}$) and optical
463 spectroscopy at 467 nm ($OCP_{R27L\text{-}Ntag}$, $OCP_{wt\text{-}Ntag}$ and $OCP_{wt\text{-}Ctag}$).

464 For the structural monitoring, accumulation of the OCP^R state was achieved by illuminating a 23 mg/ml
465 (620 μM) solution of $OCP_{wt\text{-}Ctag}$ for ~ 30 minutes at 430 nm with a 500 mW continuous LED source
466 collimated to ~ 1 cm (*i.e.* the same illumination protocol used in SAXS experiments described in the
467 previous section), providing the starting point of the kinetics, and scattering data were thereafter
468 recorded every ~ 12 s. It was established in our static SAXS measurements that formation of $OCP^R_{wt\text{-}}$
469 $_{Ctag}$ state is characterized by the presence, in the $\Delta S(q)$ difference pattern, of a negative peak at ~
470 0.05 $Å^{-1}$ and a positive peak at ~ 0.12 $Å^{-1}$ (Fig. 3*C*). Hence, we used as a proxy to evaluate the
471 structural recovery of the starting $OCP^O_{wt\text{-}Ctag}$ state the $\Delta S = S(t) - S_0$ difference signal in the 0.05 -
472 0.5 $Å^{-1}$ range, where S(t) and S_0 are the scattering patterns at a generic time (t) after switching off the
473 430 nm light and before the 430 nm irradiation procedure, respectively (Fig. S3 and Table S2). These
474 data show that structural recovery of the dimeric $OCP^O_{wt\text{-}Ctag}$ state occurs on a time scale of tens of
475 minutes, when $OCP^R_{wt\text{-}Ctag}$ is accumulated at high concentrations by prolonged illumination.

476 The spectroscopic recovery of $OCP_{R27L\text{-}Ntag}$, $OCP_{wt\text{-}Ntag}$ and $OCP_{wt\text{-}Ctag}$ was monitored in the 0.1 - 16
477 mg/ml concentration range, after accumulation of OCP^R by the same illumination protocol used in the
478 static SAXS measurements. Just after switching-off the 430 nm light at time t_0 (*i.e.* when the
479 concentration of OCP^R is at its maximum), the time evolution of the normalized absorption difference
480 $[A(t) - A(t_0)]/[A(t_{max}) - A(t_0)]$ at 467 nm was monitored, where $A(t)$ and $A(t_{max})$ are the absorption values
481 measured at a generic time t during the thermal recovery and at the time t_{max} = 5000 s, where the
482 initial OCP^O state has been 95-99 % recovered (Fig. S4), respectively. Normalization was performed
483 to enable direct comparison of data (Fig. S4) and of the fits at the various tested concentrations, viz.
484 0.1, 1.7, 3 and 16 mg/ml (Fig. S5). Alike the structural recovery, spectroscopic recovery occurs on a
485 time scale of tens of minutes, with recovery slowing down as the protein concentration increases.
486 Regardless of the concentration, however, $OCP_{R27L\text{-}Ntag}$ recovers faster than $OCP_{wt\text{-}Ntag}$, which itself
487 recovers faster than $OCP_{wt\text{-}Ctag}$. As $OCP_{R27L\text{-}Ntag}$ and $OCP_{wt\text{-}Ntag}$ differ only in their capacity to form
488 OCP^O dimers, and $OCP_{wt\text{-}Ntag}$ and $OCP_{wt\text{-}Ctag}$ only in the location of the his-tag, these observations
489 suggest that (i) the re-association of OCP^O monomers into dimers is the limiting step in the recovery
490 of $OCP_{wt\text{-}Ntag}$; and (ii) presence of a his-tag at the C-terminus negatively impacts dark-state recovery.
491 We attempted fitting the recovery data using constrained (same set of characteristic times for the four

492 concentrations) mono-to-quadruple exponential functions (see Materials and Methods), where (i) a_{ci-1}, a_{ci-2}, a_{ci-3} and a_{ci-4} are pre-exponential factors depending on the protein variant and the concentration, (ii) τ_{ci-1}, τ_{ci-2}, τ_{ci-3} and τ_{ci-4} are characteristic times describing up to four separate molecular steps. A minimum of three exponentials are needed to account for the recovery kinetics of the three OCP variants. The characteristic times derived from the $OCP_{R27L-Ntag}$ data (τ_{ci-1}= 59.8 ± 0.3 s; τ_{ci-2} = 159.1 ± 0.6 s; τ_{ci-3} = 641.7 ± 1.1 s, Table S2) are nearly half of those derived from the $OCP_{wt-Ntag}$ data (τ_{ci-1}= 94.5 ± 0.2 s; τ_{ci-2} = 356.5 ± 1.2 s; τ_{ci-3} = 1327.5 ± 4.3 s, Table S2), and no better fits are obtained by accounting for a fourth component (similar chi^2 for either dataset; Tables S2 and S3), precluding extraction of a time constant for dimerization of $OCP_{wt-Ntag}$. Nonetheless, it is presumable based on the evolution of pre-exponential factors as a function of concentration that our data inform on the contribution to recovery of various oligomeric OCP^R species, namely the monomers (a_{ci-1}; τ_{ci-1}), dimers (a_{ci-2}; τ_{ci-2}) and tetramers (a_{ci-3}; τ_{ci-3}). Indeed, the populations associated to the first and second components intersect at 0.5, at low concentration, while those of the second and third components do the same, at higher concentration (Fig. 3*D, E, F*). A three-exponential fitting procedure applied to the $OCP_{wt-Ctag}$ (Table S3) data yields longer characteristic times (τ_{ci-1}= 76.7 ± 0.2 s; τ_{ci-2} = 593.1 ± 2.1 s; τ_{ci-3} = 9517.4 ± 75 s), in line with the observed slower recovery, yet the data are better fitted (~4 times smaller chi^2, *i.e.,* a value close to those obtained for $OCP_{R27L-Ntag}$ and $OCP_{wt-Ntag}$ regardless of whether three or four exponential components are considered) by a four-exponential model (τ_{ci-1}= 51.5 ± 0.2 s; τ_{ci-2} = 209.9 ± 1.3 s; τ_{ci-3} = 946.0 ± 3.7 s; τ_{ci-4} = 14057.7 ± 68.8 s; Table S2). Presumably, the fourth component informs on OCP^O dimerization, given the comparatively low contribution of this component to the recovery signal and the expectation that presence of a his-tag at the N-terminus will challenge dimer formation in $OCP_{wt-Ntag}$, but not $OCP_{wt-Ctag}$. Alternatively, this component could underlie a step that becomes rate-limiting in the $OCP_{wt-Ctag}$, e.g. repositioning of the CTT on the CTD β-sheet. A global four exponential-fit of the three data sets, whereby the characteristic recovery times for $OCP_{R27L-Ntag}$, $OCP_{wt-Ctag}$ and $OCP_{wt-Ntag}$ were constrained to be identical and the simpler kinetics of $OCP_{R27L-Ntag}$ (no dimerization of OCP^O) accounted for by constraining to zero the population parameter a_{ci-4}, corresponding to the longest characteristic time, was unsuccessful. Our dat thus point to at least three, and in the case of $OCP_{wt-Ctag}$ fourindependent molecular steps being involved in the OCP^R to OCP^O recovery.

Kinetics of OCP^R formation and $OCP^R \rightarrow OCP^O$ thermal recovery on the ns to s time-scale.

To investigate short-live intermediate states which exist along the $OCP^O \rightarrow OCP^R$ and $OCP^R \rightarrow OCP^O$ transitions, we used ns-s timescale transient spectroscopy whereby 8 ns pulses from a 470 nm laser (5 mJ pulse energy) were employed to trigger photoactivation, and difference absorbance (ΔA) signals at 440 and 565 nm were monitored. The 440 nm probe wavelength is located at the blue edge of OCP^O absorption spectrum, and therefore informs on the depletion and recovery of this state upon

527 and after excitation by the 470 nm pulse, respectively. Conversely, the 565 nm probe is at the red
528 edge of the OCP^R absorption spectrum and thus serves as an indicator for the formation of the red
529 absorbing states, including the first probed photoproduct P_2 ($\lambda_{\Delta Amax}$ = 565 nm, with occupancy
530 proportional to the ΔA signal), OCP^R ($\lambda_{\Delta Amax}$ = 550 nm) and all OCP^R intermediate states between
531 these.

532 We first investigated $OCP_{wt\text{-}Ctag}$, $OCP_{R27L\text{-}Ntag}$ and $OCP_{wt\text{-}Ntag}$ at 12 μM concentration, *i.e.* ~ 0.18 mg/ml
533 (Fig. 5*A*), where nearly as many $OCP^O_{wt\text{-}Ctag}$ and $OCP^O_{wt\text{-}Ntag}$ are present in the monomeric form (54
534 %, *i.e.* 6.5 μM) and in the dimeric form (46 %, *i.e.* 2.79 μM (Table S4)), assuming a similar dissociation
535 constant of 14 μM for the two variants. Given this starting concentration, the pulsed nature of the
536 excitation and the low quantum yield of photoactivation, OCP^R cannot accumulate in these
537 experiments, hence the formation of OCP^R dimers and tetramers by $OCP^O_{wt\text{-}Ctag}$ and $OCP^O_{wt\text{-}Ntag}$ is
538 extremely unlikely. We examined the temperature dependence (8°-36° C) of the ΔA signals at 440
539 nm and 565 nm in $OCP_{wt\text{-}Ctag}$, with the aim to identify key intermediate states and determine their
540 associated enthalpy and entropy of activation. Experiments revealed that irrespective of temperature,
541 all kinetics recorded at 440 nm start from the same ΔA value, viz. - 2 mOD (Fig. S7), indicating that
542 depletion of the initial $OCP^O_{wt\text{-}Ctag}$ state (with ~ 0.7 % yield, as determined by Ruthenium actinometer;
543 see Materials and Methods) hardly depends on the temperature. Notwithstanding, the initial (~ 50 ns)
544 ΔA signal at 565 nm decreases with increasing temperature, amounting to 3 mOD at 8° C but only
545 1.5 mOD at 36° C (Fig. S7*A* and S7*E*). A possible interpretation is that the increased temperature
546 results in a lower yield of the red states, including the final $OCP^R_{wt\text{-}Ctag}$, due to non-adiabatic processes
547 occurring earlier than our first data point (~ 50 ns) which do not repopulate directly the dark $OCP^O_{wt\text{-}}$
548 $_{Ctag}$ state (monitored at 440 nm). Another interpretation could be that the molar extinction coefficient
549 of the OCP^R-bound carotenoid decreases with increasing temperature.

550 The ΔA signal for $OCP_{wt\text{-}Ctag}$ at 565 nm appears triphasic in the 8-36 °C range (Fig. S7*A* – S7*F*), and
551 likewise for the 440 nm ΔA signal in the 8-22 °C range (Fig. S7*C* – S7*F*). The two sets of difference
552 signals at 440 and 565 nm probe the same molecular events, since similar characteristic times and
553 activation energies can be derived from the two sets of data (Table S4 and Fig. 5*E*, respectively).
554 Hence, we opted for a global tri-exponential fitting of the 440 and 565 nm data. Note that an additional
555 fourth component intrudes into kinetics after 100 ms at 29° C and 36° C (Fig. S7*D* and S7*E*), which
556 presumably lives longer than our time window at lower temperatures. Characteristic times were
557 extracted for each step (Table S4), and Eyring plots generated from the measurements carried out at
558 different temperatures (Fig. 5*E*). The fastest component (~ 2 μs) displays an adiabatic behavior and
559 is associated with a negative change in entropy, pointing to a reorganization process that reduces the
560 complexity of the system, does not involve rupture of H-bonds or salt-bridges, and is fully fueled by
561 conformational changes that have occurred before our first time-delay, *i.e.* ~ 50 ns. The two other

562 components, characterized by characteristic times in the 0.2 - 5 and 10 - 250 ms range, respectively,
563 are both characterized by increase of the entropy (11-18 cal.mol^{-1}.K^{-1}), indicating irreversibility, and
564 display similar enthalpies of activation, viz. 18 kcal/mol (Fig. 5*E*).

565 The extent of recovery of the ΔA signal at 440 nm is slightly higher at increased temperature, with ≈
566 50 % of the initially-depleted OCP^O state (0.7 % at 50 ns) having recovered after 1 s at 8 °C, but ~ 75
567 % at 36° C (Fig. S7). Briefly, overall OCP^R yields of 0.35, 0.26, 0.25, 0.20 and 0.18 % are found at 8,
568 15, 22, 29 and 36 °C based on the 440 nm data at 500 ms, respectively. Hence, the recovery of the
569 OCP^O state somehow benefits from increased thermal energy, but is not completed after 1 s (*i.e.* the
570 ΔA signal at 440 nm is not null (Fig. S7), regardless of temperature. We interpret this data as a
571 confirmation that the limiting step in the monomeric $OCP^R_{wt\text{-}Ctag}$ → $OCP^O_{wt\text{-}Ctag}$ transition occurs on a
572 time scale longer than 1s (observed in SAXS data, Fig. S3 and Table S2 and S3). The 565 nm kinetics
573 also decay faster at higher temperatures (yields at 500 ms are 0.8, 0.44, 0.18, 0.02, 0.16 % at 8, 15,
574 22, 29 and 36 °C, respectively), indicating a lower yield for the red states (including $OCP^R_{wt\text{-}Ctag}$).
575 Surprisingly, however, the ΔA signal at 565 nm is null after 1 s at 29 °C (and negative at 36 °C), which
576 would suggest that no $OCP^R_{wt\text{-}Ctag}$ remains. These diverging results illustrate the usefulness of probing
577 photoactivation and recovery at the two extremes of OCP^O and OCP^R absorption spectra to obtain
578 meaningful insights into the complex underlying mechanisms.

579 We repeated the above-described experiments on the constitutively monomeric $OCP_{R27L\text{-}Ntag}$ mutant.
580 The 565 nm kinetics, shown in Fig. 5, are overall similar for $OCP_{wt\text{-}Ctag}$ and the $OCP_{R27L\text{-}Ntag}$ mutant.
581 From the multiexponential fits, we accordingly derive comparable characteristic times, with the main
582 difference between the two proteins differing in a two-times shorter τ_3 component for $OCP_{R27L\text{-}Ntag}$, as
583 compared to $OCP_{wt\text{-}Ctag}$ (Table S4). Thus, only the last component shows a putative influence of the
584 presence of dimers (recall that 46 % of $OCP^O_{wt\text{-}Ctag}$ is present in the form of dimers at 12 μM).
585 Accordingly, the Eyring plots for $OCP_{R27L\text{-}Ntag}$ (Fig. 5*F*) reveal analogous trends for the two first
586 components, while the τ_3 component is characterized by larger activation enthalpy and entropy. To
587 determine whether or not these differences could arise from the position of the his-tag at the N- or C-
588 terminus of the protein, we further investigated $OCP_{wt\text{-}Ntag}$ at 22° C, and compared derived
589 characteristic times with those obtained from $OCP_{R27L\text{-}Ntag}$ and $OCP_{wt\text{-}Ctag}$ (Table S4). We again
590 observed similar dynamics, with derived characteristic times and relative contributions for the three
591 steps being almost identical in $OCP_{wt\text{-}Ntag}$ and $OCP_{wt\text{-}Ctag}$. An interesting difference is, however, that
592 $OCP_{wt\text{-}Ntag}$ displays a nearly two-times increased OCP^R yield at 1 s, suggesting that dissociation of the
593 NTE from the CTD, facilitated by adjunction of an his-tag at the N-terminus, is a limiting step in
594 photoactivation of OCP. This event is yet silent in terms of changes in the absorption of the carotenoid,
595 since none of the components identifiable in the 440 and 565 nm kinetics are affected by the change
596 in tag position in $OCP_{wt\text{-}Ntag}$ and $OCP_{wt\text{-}Ctag}$.

597 Transient spectroscopy data presented so far were acquired in conditions where $OCP^{O}_{wt\text{-}Ctag}$ and
598 $OCP^{O}_{wt\text{-}Ntag}$ monomers are slightly prevalent (54 %), and differences with the constitutively monomeric
599 $OCP^{O}_{R27L\text{-}Ntag}$ were seen only for the τ_3 component. To further verify whether or not these changes
600 arise from dimerization of the protein, we repeated experiments on $OCP_{wt\text{-}Ctag}$ and $OCP_{R27L\text{-}Ntag}$ at 50
601 and 250 μM, where dimers account for 78 and 95 % of the OCP^{O} population, respectively (Fig. 5*C*
602 and 5*D*). Only the ΔA signal at 565 nm was probed. Both the initial P_2 yield at 50 ns and the overall
603 OCP^{R} yield at 0.1 s increase with concentration for $OCP_{wt\text{-}Ctag}$, but not for $OCP_{R27L\text{-}Ntag}$, indicating that
604 stabilization of the closed conformation of OCP^{O} through dimerization favors the initial steps of
605 photoactivation (Fig. S8*A* and Table S4). The characteristic times derived for the $OCP_{R27L\text{-}Ntag}$ sample
606 are only marginally affected by the increase in concentration, whereas a nearly two-fold increase in
607 τ_3 lifetime is seen for $OCP_{wt\text{-}Ctag}$ at 50 and 250 μM. Thus, these experiments confirm that the τ_3
608 component, although present also in the monomer, is affected by dimerization. Specifically, a plot of
609 τ_3 lifetime as a function of OCP dimers concentration, assuming the average τ_3 lifetime of $OCP_{R27L\text{-}}$
610 $_{Ntag}$ for zero dimer concentration, reveals a logarithmic behavior with half-maximum reached at ~ 10
611 μM dimer, corresponding to ~ 25 μM $OCP^{O}_{wt\text{-}Ctag}$ (Fig. S8*B*). It is interesting to note that regardless of
612 the sample and concentration, the τ_2 component (~ 1 ms) has an almost constant value and relative
613 contribution in all kinetics measured at 22 °C.

614

615 **Time-resolved X-ray scattering.**

616 Time-resolved X-ray scattering measurements were carried out using a pump-probe scheme with
617 view to investigate the large-scale structural changes occurring in OCP_{wt} upon photo-activation, and
618 the associated time scales. We used two variants of $OCP_{wt,}$ viz. $OCP_{wt\text{-}Ntag}$ and $OCP_{wt\text{-}Ctag}$, enabling to
619 test whether or not presence of a histidine-tag at the N- or C- terminus influences pulsed
620 photoactivation kinetics. Indeed, it has been observed that both OCP^{R} accumulation under prolonged
621 illumination and the subsequent thermal recovery are faster for $OCP_{wt\text{-}Ntag}$ than $OCP_{wt\text{-}Ctag}$ (Wilson et
622 al., in review.; Nizinski et al., in review). From our ns-s transient absorption characterization of
623 photoactivation and recovery in $OCP_{wt\text{-}Ntag}$ and $OCP_{wt\text{-}Ctag}$, it was expected that at 22° C, the two steps
624 involving large scale motions are characterized by characteristic times of ≈ 1 and ≈ 80 ms (Fig. 5).
625 Hence, time delays (Δt) between the pump optical-laser pulse and the probe X-ray pulse ranged from
626 15 μs to 200 ms. Experiments were performed at 23 mg/ml (620 μM) $OCP_{wt\text{-}Ntag}$ and $OCP_{wt\text{-}Ctag}$, *i.e.* a
627 concentration at which dimers account for ~ 98 % of the protein.

628 The experimental setup designed for this experiment is described in the Experimental Section and
629 involves the circulation of a large volume of sample across the X-ray beam to minimize cumulative X-
630 ray damage during the experiment. The circulation speed was set so as to ensure that the sample is

631 kept in the pump–probe intersection area during a pump–probe sequence, but refreshed between
632 two consecutive pump pulses. We verified that with this setup, the same difference scattering signal
633 observed in static SAXS experiments could be obtained upon continuous illumination of the sample
634 reservoir by a 500 mW LED source emitting at 430 nm. The LED illumination was prolonged until the
635 photoinduced change in scattering signal was stable. The resulting difference scattering pattern is
636 similar to that produced from our static measurements, *i.e.,* it features a negative peak at 0.05 $Å^{-1}$ and
637 a positive peak at 0.12 $Å^{-1}$ (Fig. 3*C*). This control indicates that the use of a different continuous
638 illumination setup at a different beamline does not result in shifts in the difference scattering signal
639 (Fig. 6*A*).

640 With intention to determine the extent to which photoactivation can be increased by successive re-
641 excitations within the pulse, we first measured the 'light' (laser-on) minus 'dark' (laser-off) difference
642 scattering signal at Δt = 1 ms, using two different laser pulse durations, viz. 5 and 450 ns. This required
643 using two different lasers, emitting at 430 and 527 nm, respectively. At these wavelengths, the
644 extinction coefficients of OCP^O are similar (≈ 35 000 M^{-1} cm^{-1}), suggesting that the OCP^R formation
645 quantum yield should be similar and that an increase in the difference signal at 527 nm would stem
646 from successful re-excitation within the 450 ns pulse. Both pulse durations are indeed longer than the
647 time necessary to recover the electronic ground state (~ 20 ps) (25), (53). A pulse power density of 3
648 mJ.mm-2 was chosen, affording the delivery of ~ 75 photons per chromophore across the pulse,
649 corresponding to a photon every 0.06 and 5 ns for the 5 and 450 ns pulse durations, respectively.
650 The two 'light' (laser-on) minus 'dark' (laser-off) difference scattering patterns at Δt = 1 ms both feature
651 a negative peak in the small angle region up to ≈ 0.1 $Å^{-1}$, but the amplitude of the peak does not vary
652 significantly, indicating that stretching the pulse up to 450 ns does not improve the photoactivation
653 extent (Fig. 6*A*). Thus, OCP molecules that have not engaged towards formation of a red state (P_1)
654 and are back to the ground state (25) cannot be re-excited within the 450 ns pulse. Given the fact that
655 these molecules do not show a difference signal in transient absorption spectroscopy experiments –
656 meaning that the carotenoid is back in the orange state and therefore presumably H-bonded to the
657 protein scaffold – their inability to re-enter a photocycle could be rooted in the fact that some protein
658 residues, which are important for photoactivation but do not influence the spectrum, have not returned
659 yet to their initial conformation after 450 ns. We refer to this *hitherto* undescribed intermediate state,
660 which accounts for 99.3 % of the OCP^O population upon pulsed illumination, as the OCP "numbed-
661 state", abbreviated OCP^{NS}. To estimate an upper boundary for the lifetime of this intermediate, the
662 repetition rate (1 kHz) of the 527 nm laser, coupled with a synchronized chopper/shutter system, was
663 used to measure time-resolved patterns at a time delay of 100 ms excitation by an increasing number
664 of consecutive pulses spaced by 1 ms. The scattering difference signal (laser-on minus laser-off) was
665 then integrated in the 0-0.15 $Å^{-1}$ range and plotted as a function of the number of pulses (Fig. 6*B*).
666 The signal increases linearly with the number of pulses up to 5 pulses for $OCP_{wt\text{-}Ntag}$ and up to 10

667 pulses for $OCP_{wt\text{-}Ctag}$, after which a plateau is observed, presumably due to concomitant recovery of
668 the dark state structure (see below). Thus, the lifetime of the non-re-excitable OCP^{NS} can be estimated
669 to lie between 450 ns and 1 ms. Irrespectively, comparison of the two time-resolved difference signals
670 with the static difference scattering signal shows that the shape of the difference pattern generated
671 by pulsed excitation does not coincide with that obtained by stationary illumination. In particular, the
672 position of the negative peak differs, and the positive peak at ~ 0.12 $Å^{-1}$ is absent (Fig. 6*B*).

673 A complete time-resolved dataset was measured at time delays between 15 µs and 200 ms. Data for
674 $OCP_{wt\text{-}Ctag}$ are shown in Fig. 6*C*, while analogous results are obtained for $OCP_{wt\text{-}Ntag}$. Fig. 6*C*
675 demonstrates that substantial changes in the scattering patterns are (i) already visible after 15 µs, (ii)
676 maximized before 1 ms, and (iii) substantially damped by 200 ms. To further investigate the kinetics
677 of the scattering signal changes, the time-resolved scattering dataset was analyzed by the singular
678 value decomposition (SVD) method (see Materials and Methods), which revealed that the entire
679 dataset can be described by a single time-independent basis pattern (continuous line in Fig. 6*C*). In
680 other words, no other intermediate state than that responsible for this basis pattern is visible in our
681 data. It must be noted that the difference between the time-resolved and static difference signals, *i.e.*
682 the shift in q-value of the negative peak and the absence of a positive peak, is observed for all
683 recorded time delays (15 µs-200 ms). Notwithstanding a rough estimation of the photoactivation
684 extent by ns excitation can be obtained from the amplitude of the time-resolved difference signal
685 compared to the static signal, which gives a value of ~ 1.8 % (Fig. 6*A*). Difference patterns in (Fig.
686 6*C*) were integrated in the 0 - 0.15 $Å^{-1}$ range and the results as a function of time are shown in (Fig.
687 6*D*) for both $OCP_{wt\text{-}Ntag}$ and $OCP_{wt\text{-}Ctag}$. The integrated intensity starts decaying between 1 and 10 ms
688 in $OCP_{wt\text{-}Ntag}$, and between 10 and 100 ms in $OCP_{wt\text{-}Ctag}$, indicating a recovery of the dark state in
689 these timescales, in full agreement with the results in Fig. 6*C*. Thus, large scale conformational
690 changes start occurring as of ~ 10 µs, maximize at 1 ms, and revert with apparent characteristic times
691 (*i.e.* time at half-maximum amplitudes) of ~ 37 and ~ 150 ms for $OCP_{wt\text{-}Ntag}$ and $OCP_{wt\text{-}Ctag}$, respectively.

692 It is tantalizing, but difficult, to propose an interpretation for our observations. It has been proposed
693 earlier that the first large-scale conformational change (~ 1 ms time scale) occurring in OCP post-
694 excitation is the detachment of the NTE from the CTD β-sheet, possibly concomitant with a
695 repositioning of the CTT, followed by dissociation of the two domains (25, 27). Given the quantum
696 yield of OCP and the fact that our TR-SAXS experiment was carried out at 23 mg/ml (620 µM), where
697 dimers account for ~ 98 % of the sample, it is yet extremely unlikely that two monomers in the same
698 dimer would have been photoexcited by the same pulse (probability is ≈ $1e^{-5}$). Furthermore, since the
699 NTE is involved in the dimerization interface, domain dissociation would have to await
700 monomerization. Hence, it is most probable that the conformational change probed in our experiment

701 is neither dimer or domain dissociation, but rather a subtle conformational change occurring in one of
702 the two monomers in a dimer.

703

704 **Discussion (4273 words)**

705 In the present work, we used TR visible spectroscopy, as well as static and TR X-ray scattering to
706 investigate the structural changes – including changes in quaternary structure – accompanying
707 photoactivation of the orange carotenoid protein (OCP). It was repeatedly observed that OCP
708 crystallizes as a dimer, yet it had remained elusive whether or not this interface is functional given the
709 high concentration of the protein in crystals, viz. ≈ 23 mM. Mutation of a single conserved residue at
710 the crystalline dimerization interface results in the loss of the ability to dimerize, suggesting that the
711 dimer could indeed be physiological (10). Collection and analysis of static X-ray scattering patterns
712 of dark-adapted $OCP_{wt\text{-}Ctag}$ as a function of concentration confirm the *in vitro* existence, already
713 suggested in the literature (20, 21, 23, 24, 28, 54), of a dimer which becomes predominant at
714 concentrations ≳ 1 mg/ml (Fig. 3*B*, Fig. 4 and Fig. S1*B*). Our SAXS titration data (Kd ~ 14 μM) is in
715 accordance with (i) previous results from native mass spectrometry experiments, reporting the
716 presence of OCP^O dimers at concentration as low as 3 μM (20); (ii) the recent assertion based on
717 SAXS and SANS data that OCP^O resides in the same state at 1 and 65 mg/ml (*i.e.* 28 μM and 1.8
718 mM) (21, 22); and (iii) the dissociation constant that can be derived from size exclusion
719 chromatography results presented in Fig. 3 of Muzzopappa et al. (10), *i.e.*, ≈ 0.6 mg/ml (17 μM),
720 provided that we use the same extinction coefficient at 490 nm to estimate protein concentrations.

721 Analogous concentration-dependent analyses of static X-ray scattering patterns collected after
722 accumulation of $OCP^R_{wt\text{-}Ctag}$ and $OCP^R_{R27L\text{-}Ntag}$ by 30 min irradiation at 430 nm suggest that they are
723 also prone to oligomerization. Indeed, for both proteins, not only is the scattering signal different
724 between the dark-adapted (OCP^O) and light-adapted (OCP^R) states, but this difference evolves as a
725 function of concentration. Remarkably, $OCP^R_{R27L\text{-}Ntag}$ and $OCP^R_{wt\text{-}Ctag}$ display similar P(r) (Fig. 2*F*) and
726 Rg (Fig. 3*A*) at the various tested concentrations, suggesting that they form the same OCP^R state(s).
727 The high-concentration (10.5 mg/ml) difference-scattering patterns between the light- and dark-
728 adapted states, *i.e.* $\Delta S(q)_{R27L\text{-}Ntag}$ and $\Delta S(q)_{wt\text{-}Ctag}$, are characterized by the presence of a negative
729 peak (at 0.07 and 0.05 $Å^{-1}$, respectively) and a positive peak (at 0.14 and 0.12 $Å^{-1}$, respectively).
730 These peaks respectively signal the loss and gain of interatomic distances in the OCP samples, upon
731 illumination and their transition from the OCP^O to the OCP^R state. Given that $OCP^R_{R27L\text{-}Ntag}$ and
732 $OCP^R_{wt\text{-}Ctag}$ form the same OCP^R species, the observation that the negative and positive peaks are
733 found at different q-values in the $\Delta S(q)_{R27L\text{-}Ntag}$ and $\Delta S(q)_{wt\text{-}Ctag}$ difference patterns can be rationalized
734 by the fact that their dark-adapted states differ – $OCP^O_{R27L\text{-}Ntag}$ being present as a monomer, whereas
735 $OCP^O_{wt\text{-}Ctag}$ features a dimer.

736 The molecular envelopes reconstructed from the OCP^R data suggest that OCP^R dimers form as of
737 0.7 mg/ml (20 μM), while tetramers form above 3.5 mg/ml (100 μM), becoming predominant at
738 concentrations greater than 10.5 mg/ml (300 μM) (Fig. 3*B* and 4). The observation that the R27L

739 mutant also forms OCP^R dimers and tetramers suggests that the dimerization interfaces of OCP^O and
740 OCP^R do not overlap. Based on this hypothesis, and on knowledge from the literature, we were able
741 to build tentative models for OCP^R dimers and tetramers. The models notably assume that : i) OCP^R
742 tetramers form from the coalescence of two OCP^R dimers; ii) interactions between OCP^R monomers
743 in a dimer and between OCP^R dimers in a tetramer involve the same interface in the two interacting
744 proteins; iii) residues involved in assembly of OCP^R into dimers and tetramers are not exposed in the
745 dark OCP^O dimer (51, 52); and iv) OCP^R dimers assemble via their CTD, so that their two NTD are
746 exposed and free to interact with PBS via R155 (50), while the OCP^R tetramers form from an
747 interaction between two NTD in the OCP^R dimer, as seen in the crystal structures of HCP homologues
748 (39, 40), (41, 50). Our model for the $OCP^R_{wt\text{-}Ctag}$ dimer is in overall agreement with that proposed
749 earlier (21), featuring two monomers associated by their CTD at an interface reminiscent of that
750 observed at the A-type interface in the apo-*Anabaena* CTDH crystal structure. Of note, helices αN (or
751 CTT) and αA (or NTE), which sit aside one another on the external side of the β-sheet but detach
752 upon photoactivation (9), were considered as disordered in OCP^R and therefore not included in our
753 $OCP^R_{wt\text{-}Ctag}$ dimer model. To account for the known exposure, in OCP^R, of the face of the NTD that
754 interacts with the CTD in OCP^O, each NTD was rotated by 180° and further translated by a few Å to
755 avoid clashes with the CTD. The exposed face of the NTD features R155, which tethers the NTD to
756 the CTD via H-bonding to E244 in OCP^O, but is essential for the interaction of OCP^R with the PBS.
757 To fit the elongated density of the tetramer, and account for the unavailability for interaction of the
758 CTD in the $OCP^R_{wt\text{-}Ctag}$ dimer, we assembled two such dimers by their NTD, using as a template the
759 dimerization interface observed in all three currently available crystal structures of the homologous
760 Helical Carotenoid Proteins (HCPs) (pdb ids: 5FCX and 6MCJ (39, 40)). This interface features the
761 residue equivalent to R155 in OCP; hence, in our model, the two dimers in an OCP^R tetramer interact
762 by the same face known to bind to the PBS. In other words, in all OCP^R tetramers, only two NTD
763 faces are available to bind and quench the PBS.

764 We used a combination of optical spectroscopy and X-ray scattering to investigate OCP^R to OCP^O
765 thermal recovery and determine whether or not it is influenced by oligomerization processes. First,
766 we monitored the structural recovery of the $OCP^O_{wt\text{-}Ctag}$ state, following accumulation of the $OCP^R_{wt\text{-}}$
767 $_{Ctag}$ state by prolonged illumination at 430 nm. The difference scattering pattern features a positive
768 and a negative peak (Fig. 3*C*), which together signs for the disappearance of the starting $OCP^O_{wt\text{-}Ctag}$
769 state and the concomitant appearance of $OCP^R_{wt\text{-}Ctag}$ states. Hence, the time evolution of the
770 difference signal in the 0.05 -0.5 $Å^{-1}$ q-range was used to follow the overall recovery, and is best fitted
771 by a single exponential with a characteristic times $\tau\Delta S(q)$ overall of ~ 4160 s (Fig. S3). The fact that
772 this kinetics can be fitted by just a single exponential can be explained by technical and physical
773 considerations: (i) the low temporal resolution (≈ 20 s) conceals to reveal characteristic times shorter
774 than hundreds of seconds; (ii) the comparatively short time range explored obscures the full

775 description of the recovery kinetics; (iii) the low-resolution structural probe used in our study is not
776 sensitive to the presence of intermediates localized at the chromophore level.

777 Hence, further insights in the OCP^R to OCP^O thermal recovery were attained by resorting to
778 spectroscopy at various protein concentrations. First, we accumulated OCP^R by prolonged
779 illumination at 430 nm, and monitored recovery of OCP^O by following absorption at 467 nm.
780 Regardless of the sample, we found that the recovery time markedly increases as a function of
781 concentration, in full agreement with the indication from static X-ray scattering data that both OCP^O
782 ($OCP_{R27L\text{-}Ntag}$, $OCP_{wt\text{-}Ntag}$ and $OCP_{wt\text{-}Ctag}$) and OCP^R ($OCP_{R27L\text{-}Ntag}$, $OCP_{wt\text{-}Ntag}$ and $OCP_{wt\text{-}Ctag}$)
783 oligomerize. Indeed, the more oligomeric states present, the higher the overall energy barrier for a
784 full recovery of the starting dark OCP^O to occur, and therefore the longer it will take for full recovery
785 to be befall. Irrespective of the assayed concentration, the spectroscopic recovery of $OCP^O_{wt\text{-}Ntag}$ was
786 found to be slower than that of $OCP^O_{R27L\text{-}Ntag}$, indicating that the reassembly into dimers of OCP^O
787 monomers is the step that limits $OCP^O_{wt\text{-}Ntag}$ recovery. Likewise, the recovery of $OCP^O_{wt\text{-}Ctag}$ was slower
788 than that of $OCP^O_{wt\text{-}Ntag}$, indicating that presence of the his-tag at the C-terminus adversely affect
789 recovery of the dark-adapted state. We plotted the pre-exponential factors as a function of
790 concentration to follow the evolution of the associated populations (Fig. 3*D-F* and Fig. S6). Focusing
791 first on results from the three-exponential fits, we observe a similar evolution as a function of
792 concentration in the three samples: (i) the amplitude of the fastest component ($a_{ci\text{-}1}$, $\tau_{ci\text{-}1}$) decreases;
793 (ii) the amplitude of the intermediate component ($a_{ci\text{-}2}$, $\tau_{ci\text{-}2}$) initially increases but then decreases; (iii)
794 the amplitude of the slowest component ($a_{ci\text{-}3}$, $\tau_{ci\text{-}3}$) steeply increases. The observation of intersections
795 at 0.5 population between amplitudes of rising and declining components is suggestive of a link
796 between their relative populations. The populations of the first and second components feature such
797 an intersection at concentrations of ~ 0.7 and 1.8, in $OCP_{R27L\text{-}Ntag}$ (Fig. 3*D*) and $OCP_{wt\text{-}Ntag}$ (Fig. 3*E*),
798 and at 6 mg/ml, in $OCP_{wt\text{-}Ctag}$ (Fig. S6*C*). Assuming that the first and second components inform on
799 the contribution to recovery of OCP^R monomers and dimers, a possible explanation is that presence
800 of the his-tag at the C-terminus challenges dimerization of OCP^R in $OCP_{wt\text{-}Ctag}$, elevating the apparent
801 dissociation constant. For $OCP_{R27L\text{-}Ntag}$ and $OCP_{wt\text{-}Ntag}$, we furthermore see that the population of third
802 component intersects those of the first (at ~ 1.7 and ~ 7 mg/ml, respectively) and second components
803 (at ~ 9.5 and ~ 14.5 mg/ml, respectively), with the latter occurring at a population of 0.5. Assuming
804 that the slowest component informs on the contribution of OCP^R tetramers to the recovery signal, this
805 observation would be suggestive of a facilitated accumulation of OCP^R tetramers in $OCP_{R27L\text{-}Ntag}$,
806 compared to the $OCP_{wt\text{-}Ntag}$, possibly due to elimination of a competition between the dark-adapted
807 dimerization and light-adapted tetramerization interfaces. Indeed, both are localized in the NTD of
808 $OCP_{wt\text{-}Ntag}$. In the $OCP_{wt\text{-}Ctag}$ sample, we do not see intersections of the slowest component amplitude
809 with those of others components, when results of the three-exponential fit are considered. However,
810 a much better agreement is obtained when the $OCP_{wt\text{-}Ctag}$ data are fit with four-exponentials (Tables

811 S2 and S3), yielding a chi^2 comparable to that obtained with three exponentials for $OCP_{R27L\text{-}Ntag}$ and
812 $OCP_{wt\text{-}Ntag}$. Plotting the four amplitudes as a function of concentration, the same observations can be
813 made for the $OCP_{wt\text{-}Ctag}$ (Fig. 3*F*), *i.e.,* intersections at 0.5 population can be seen for the first and
814 second component at ~ 1.7 mg/ml, and for the second and third component at ~ 10 mg/ml. The
815 population of the additional fourth component, characterized by a characteristic time in the order of ~
816 4 hours (14057.7 ± 68.8 s), varies from ~ 0.04 to 0.1 with increasing concentrations, indicating that
817 the contribution of this rate-limiting step to the recovery signal is small. We see two possible
818 explanations for the presence of this additional component. A first hypothesis is that it informs on the
819 dimerization of $OCP^O_{wt\text{-}Ctag}$ monomers, which due to absence of a tag at the N-terminus would
820 reassemble faster than $OCP^O_{wt\text{-}Ntag}$, explaining that a characteristic time could be extracted for the
821 former, but not for the latter, in our experiments (t_{max} = 5000 s). Another hypothesis is that the
822 additional component informs on a step that is dramatically slowed down in $OCP_{wt\text{-}Ctag}$, compared to
823 $OCP_{wt\text{-}Ntag}$, e.g. the reattachment of the CTT to the F-side of the CTD β-sheet. Indeed, the CTT is
824 longer and presumably more flexible in $OCP_{wt\text{-}Ctag}$, compared to $OCP_{wt\text{-}Ntag}$. Our data do not allow to
825 favor one hypothesis over the other. However, the doubling of the characteristic times extracted for
826 $OCP_{wt\text{-}Ntag}$, compared to $OCP_{R27L\text{-}Ntag}$, provides circumstantial evidence that dimerization of the dark-
827 adapted $OCP^O_{wt\text{-}Ntag}$ is the limiting step in its recovery. Therefore, we favor the first hypothesis. We
828 accordingly propose that our recovery data inform on four molecular steps (Fig. 7) involved in the
829 concentration-dependent OCP^R to OCP^O thermal recovery: (i) the transition from monomeric OCP^R
830 to OCP^O, characterized by a characteristic time $\tau_{ci\text{-}1}$ = 50-100 s ; (ii) the dissociation of OCP^R-dimer
831 into OCP^R-monomers, characterized by a characteristic time $\tau_{ci\text{-}2}$ = 1 60-600 s and a dissociation
832 constant in the order of ≈ 1-2 mg/ml, depending on the considered OCP variant (≈ 30-40 μM); (iii) the
833 dissociation of OCP^R-tetramers into OCP^R-dimers, characterized by a characteristic time $\tau_{ci\text{-}3}$ = 640-
834 950 s and a dissociation constant in the order of ≈ 10 mg/ml (~ 280 μM); (iv) the re-association of
835 OCP^O-monomers into OCP^O-dimers, characterized by a characteristic time $\tau_{ci\text{-}4}$ > 14 057 s and a
836 dissociation constant in the order of ≈ 0.5 mg/ml (~ 14 μM). That OCP^O dimer formation is slowed
837 down in $OCP_{wt\text{-}Ntag}$, compared to $OCP_{wt\text{-}Ctag}$, could result from presence of a his-tag at the N-terminus,
838 *i.e.,* in the vicinity of the OCP^O dimerization interface.

839 To obtain additional insights into molecular events occurring on shorter time scales, we used pulsed
840 ns illumination to generate OCP^R (with a yield of ≈ 0.7 %), and monitored the ns-s timescale evolution
841 of the difference absorption signal (ΔA) at the blue and red edges of the OCP^O (440 nm) and OCP^R
842 (565 nm) absorption spectra, respectively. The use of the two wavelengths was justified by our need
843 to obtain insights into both the recovery of the OCP^O state (ΔA440 nm) and the formation and
844 disappearance of OCP^R and preceding red intermediates (ΔA565 nm). The wild type $OCP_{wt\text{-}Ntag}$ and
845 $OCP_{wt\text{-}Ctag}$ were investigated, as well as the constitutively monomeric $OCP_{R27L\text{-}Ntag}$ mutant. Regardless
846 of the OCP sample, we could identify three intermediate states with characteristic times of ~ 2 μs, ~

847 1 ms and ~ 40-200 ms, respectively, at 22° C. The characteristic times derived from $OCP_{wt\text{-}Ntag}$ and
848 $OCP_{wt\text{-}Ctag}$ data are nearly identical, indicating that the presence of the his-tag does not influence the
849 dynamics probed at the carotenoid level on the ns-s time scale. Nonetheless, a higher OCP^R yield
850 was found for $OCP_{wt\text{-}Ntag}$, demonstrating influence of the tag on a step that is not rate-limiting, and
851 whose contribution to photoactivation and recovery is silent from the spectroscopic perspective. In
852 these experiments, carried out at 12 μM concentration where the dimeric form accounts for 46% of
853 the wt proteins, the first and second components were found to not vary as a function of the protein
854 variant, while a two-times reduced characteristic time was found for the third component in the
855 constitutively monomeric $OCP_{R27L\text{-}Ntag}$. Additional experiments carried out at 50 and 250 μM
856 concentrations of $OCP_{R27L\text{-}Ntag}$ and $OCP_{wt\text{-}Ctag}$, where the prevalence of $OCP_{wt\text{-}Ctag}$ dimers are 78 and
857 95 %, respectively, revealed a marginal influence of concentration on the characteristic times
858 determined for $OCP_{R27L\text{-}Ntag}$, but a two-fold increase in the lifetime of the third component $\tau_{ci\text{-}3}$ for
859 $OCP_{wt\text{-}Ctag}$. A plot of the τ_3 characteristic time as a function of dimer concentration, using for zero
860 concentration the average value from $OCP_{R27L\text{-}Ntag}$ measurements at the 12, 50 and 250 μM (*i.e.* 54.8
861 ± 7.7 ms), shows a logarithmic shape, with a dimer concentration of ~ 10 μM (corresponding to an
862 overall $OCP_{wt\text{-}Ctag}$ concentration of ~ 20 μM) at half maximum (Fig. S8*B*). This result establishes that
863 the presence of dimers influences component τ_3 in a concentration dependent fashion, but neither τ_1
864 or τ_2. The data also show that the presence of dimers does not benefit the overall $OCP^R_{wt\text{-}Ctag}$ yield,
865 despite that of the initial P_2 intermediate rising with increased $OCP_{wt\text{-}Ctag}$ concentration (Fig. S8*A*). To
866 obtain further insights into the enthalpic and entropic contributions to the formation of each of the
867 three states, we furthered our analysis by carrying out experiments at various temperatures in the 8-
868 36 °C range (Fig. 5*B* and Fig. S7). We found that in both $OCP_{wt\text{-}Ctag}$ and $OCP_{R27L\text{-}Ntag}$, the first
869 intermediate – whose associated characteristic time hardly varies among proteins and concentrations
870 – is adiabatically formed, *i.e.* with no exchange of heat (Fig. 5*E* and 5*F*). Thus, all the energy
871 necessary for the formation of this intermediate is funneled into the protein scaffold before 50 ns, *i.e.*
872 the first data point in our ns-s time span. The fact that no enthalpic contribution is associated with this
873 component indicates that no H-bond or salt-bridge forms nor breaks, upon accumulation of this
874 intermediate, while the observation of a negative entropic contribution suggests a reduction in the
875 complexity of the system. Hence, component τ_1 could underlie the multi-step translocation of the
876 carotenoid from the NTD/CTD interface into the NTD. As to the two other components, τ_2 and τ_3, they
877 are associated with similar enthalpies of activation (~ 18 $kcal.mol^{-1}$) in $OCP_{wt\text{-}Ctag}$, whereas a slightly
878 larger value is found for τ_3 (~ 26 $kcal.mol^{-1}$) as compared to τ_2 (~ 20 $kcal.mol^{-1}$) in $OCP_{R27L\text{-}Ntag}$. This
879 difference in enthalpy could be rooted in the absence of dimers in the $OCP_{R27L\text{-}Ntag}$ sample, as we
880 have seen that the τ_3 component – but not the τ_2 component – is affected by the presence of these.
881 It is of note that the activation energy associated to the monomeric OCP^R to OCP^O transition after
882 prolonged illumination is 38-42 $kcal.mol^{-1}$ (10, 55), *i.e.* roughly the sum of the activation energies
883 determined for the τ_2 and τ_3 components.

884 Time-resolved SAXS/WAXS on the 15 μs – 200 ms timescale allowed us to shed partial light on the
885 structural changes associated with the OCP photocycle. Pulsed illumination results in a negative peak
886 at ~ 0.03 $Å^{-1}$ in the 'light'-minus- 'dark' ΔS(q) pattern, with this peak being already present at 15 μs,
887 maximizing before 1 ms, and starting to decrease as of 10 ms and 100 ms in $OCP_{wt\text{-}Ntag}$ and $OCP_{wt\text{-}}$
888 $_{Ctag}$, respectively. Hence, our data demonstrate that the first large scale conformational changes
889 associated with OCP photoactivation take place on the tens of μs time scale (15 μs), and that
890 reversion of these changes is influenced by the localization of the his-tag in the protein. Both transient
891 absorption spectroscopy and TR-SAXS required to work at comparatively high OCP concentration,
892 with ~ 46 % of the protein in the dimeric state at the lowest concentration tested in spectroscopy
893 experiments, and more than 98 % dimers at the highest concentration tested in spectroscopy
894 experiments or used in TR-SAXS/WAXS experiments. Thus, the two techniques probe the same
895 events occurring in similar OCP samples from the structural and the spectral perspectives, thereby
896 informing independently on the fate of the protein scaffold and of the carotenoid during
897 photoactivation, respectively. Caution must be taken when trying to jointly interpret such data hence
898 reader discretion is advised as other interpretations that those proposed herein could exist to explain
899 the two sets of data. The TR-SAXS/WAXS data is sensitive to structural changes regardless of where
900 they occur in the protein, but is too low-resolution to afford information on the carotenoid position and
901 on non-predominant species. Given that the probability that two monomers in a dimer can be activated
902 by the same pulse is ≈ $1e^{-5}$, this means that our TR-SAXS experiment cannot probe the formation of
903 OCP^R, but only that of the predominant non-productive intermediate state. This is at variance with our
904 spectroscopy data which informs on the formation of all red-shifted intermediates – productive (OCP^R,
905 offset at 0.5 s) and unproductive alike – but the spectroscopy is blind to structural changes that do
906 not affect the local environment of the carotenoid. Hence, structural and spectroscopic transitions
907 may be asynchronous, and they should be considered independently. With keeping this in mind, we
908 can propose the following sequence of events for the OCP photocycle based on ours as well as others
909 results (Fig. 8). It is known from the literature that upon absorption of the actinic photon, a S_2 state
910 forms which decays within ps into three states: the S_1 and ICT excited states and S*, which could
911 either be an excited state (25) or a vibrationally-hot ground state (56). It has been proposed that S*
912 is the precursor of P_1, a photoproduct characterized by rupture of the H-bonds between the carotenoid
913 and the protein scaffold and which displays a lifetime of ≈ 50 ns. Thereafter, the carotenoid debuts its
914 migration from the NTD/CTD interface into the NTD, first forming photoproduct P_2, after repositioning
915 at the NTD/CTD interface, and then P_2', after completing migration across the NTD. Clearly, and as
916 noted already by Konold et al. (25), this migration of the carotenoid must be accompanied by changes
917 in the relative orientation of helices αC, αE and αG, which harbor the carotenoid-tunnel bottleneck-
918 residues L37, M83 and M117. Eventually, these changes will propagate to the αG-αH loop and to
919 E34, at the kink between αB and αC, resulting in an opening of the carotenoid tunnel across the NTD
920 wall and in the formation of P_3, wherein the β2 ionone ring of the carotenoid is exposed to the solvent

921 – possibly as in the structure of the isolated NTD with canthaxanthin (18). We suppose that the first
922 step identified in our transient absorption spectroscopy (~2-3 μs) and TR-SAXS (< 15 μs) experiments
923 corresponds to the P_2' to P_3 transition, in line with (Konold et al. (25). Failed bridging of the bottleneck
924 (L37, M83, M117) is sanctioned by rapid back-migration and re-binding to H-bonding partners in the
925 CTD, *i.e.* partial recovery of OCP^O from P2', as evidenced by the fact that the decrease in ∆A565 nm
926 is mirrored by an increase in ∆A440 nm (Fig. S7). The next spectroscopically-visible step occurs on
927 the ~1 ms time scale, and is characterized by a large decrease in ∆A565 nm, that is not accompanied
928 by a similarly-extended increase in ∆A440 nm. Hence, only limited recovery of the OCP^O state occurs
929 on this time-scale, where TR-SAXS data furthermore show that no large structural changes occur.
930 Therefore, we presume that this spectroscopic step can be attributed to a back-migration, in a fraction
931 of P_3 intermediates, of the carotenoid into the tunnel. The back-migration would only be partial
932 because of the opening at both end of the carotenoid tunnel in the NTD. Our TR-SAXS data suggest
933 that depending on whether the his-tag is present at the N- or C-terminus, the dimeric P_3 intermediate
934 reverts to the OCP^O state, with characteristic times of 37 and 150 ms. This structural recovery could
935 ensue the back-migration of the carotenoid on the 1 ms time scale, *i.e.*, the two steps would be
936 decoupled. What is clear is that we do not see a large conformational change, such as detachment
937 of the NTE or CTT, occurring on the ~ 1 ms time scale, as proposed earlier (25); this could either
938 indicate that these structural steps occur latter in the photoactivation mechanism, or that TR-SAXS is
939 insensitive to structural changes occurring in only a sub-percent fraction of probed molecules. The
940 last spectroscopic transition visible in our data occurs on the 200 ms time scale, and is again
941 characterized by a large drop in ∆A565 nm that is not mirrored by a similarly-scaled increase in ∆A440
942 nm. Recalling that this step displays the same activation energy as that occurring on the ≈ 1 ms time
943 scale and that its characteristic time increases with the OCP concentration, we propose that it as well
944 signs for the back migration of the carotenoid into the carotenoid tunnel, yet this time in an
945 intermediate wherein the NTE (and possibly the CTT) has (have) detached from the CTD. Indeed,
946 since the NTE is involved in the dimerization interface, the probability that it detaches will decrease
947 (and therefore the overall time taken for the detachment to happen in an ensemble of photoactivated
948 OCP molecules, increase) as the amount of OCP dimers augments. Accordingly, we further pose that
949 NTE detachment is a prerequisite to dimer dissociation, which itself must precede separation of the
950 two domains. In other words, for OCP^O dimers to yield monomeric OCP^R, formation of P_3 must occur
951 in each of the two monomers and the dimeric P_3 fall apart into its monomeric counterpart, before the
952 reaction can further proceed. Given the low quantum yield, and our finding that P_3 starts recovering
953 the OCP^O state on the time scale of 37 and 150 ms in N-tagged and C-tagged dimers, respectively,
954 photoactivation of dimers would thus be achievable only in experiments where one photon is delivered
955 per chromophore every few ms. This is for example the case in our continuous illumination
956 experiments where, by illumination of a 23 mg/ml (620 μM) solution of OCP with a 500 mW LED
957 emitting at 430 nm, we estimate that 1 photon is delivered per chromophore every 10 - 30 ms. In this

958 context, it is interesting to note that the initial steps of photoactivation (specifically, the formation of
959 P_2) are favored by dimerization, possibly due to an increased stiffness of monomers in dimers that
960 would benefit productive excitation (formation of P_1, and thence P_2) and migration along the
961 carotenoid tunnel ($P_{2'}$). The overall OCP^R yield, however, is not drastically improved, as expected
962 given the above considerations.
963
964 The most unexpected finding from our TR-SAXS/WAXS experiment concerns the existence of a
965 'numbed' OCP intermediate, OCP^{NS}, formed upon non-productive laser excitation and decay to the
966 ground-state, which remains non-re-excitable up to the μs time scale (Fig. 6*B* and 8). Evidence for
967 the existence of this state was obtained serendipitously as we attempted to increase the extent of
968 photoactivation by distribution of actinic photons in a longer pulse. This attempt was infructuous,
969 indicating that the ground state OCP^O structure formed after excitation remains non-photoactivatable
970 for at least 0.5 μs, in line with the previous report that increasing the power of ns pulses does not
971 result in a higher photoactivation yield (13). By use of a multi-pulse approach, whereby re-excitation
972 was triggered every 1 ms for up to 30 pulses reveals an increase of the difference scattering signal,
973 we were able to estimate the lifetime of OCP^{NS} to lie between 450 ns and 1 ms. Hence, in the case
974 of OCP^O dimers, the time window for absorption of an actinic photon by the second monomer in a
975 dimer is 0.5 μs – 100 ms. Any photon that arrives before 0.5 μs is set to be unproductive, while any
976 photon that arrives after 100 ms will hit a dimer wherein both monomers are structurally back in the
977 starting state (Fig. 8).
978
979
980
981

982 **Conclusion (264 words)**

983 The emerging picture from our study suggests that oligomerization partakes in the regulation of the
984 OCP photocycle, both at the level of OCP^O and OCP^R. Whether or not these findings have implications
985 regarding the biological function depends on the local concentration of OCP in the vicinity of
986 cyanobacterial thylakoid membranes; yet the observation that the mutation of a single conserved
987 amino-acid at the OCP^O dimerization interface results in monomerization of the protein is a strong
988 argument in favor of a functional role for OCP^O dimers. The dissociation constant of OCP^O was
989 estimated to be 14 μM, and that of OCP^R dimers to be similar, whereas the dissociation constant of
990 OCP^R tetramers is likely to fall in the 3.5 mg/ml – 10.5 mg/ml concentration range. Models based on
991 our static SAXS data suggest that in OCP^R dimers and tetramers alike, only two NTD are exposed
992 and thus capable of binding to the PBS to perform their energy-quenching function. Should these
993 models be correct, one could infer that oligomerization is a means by which a plateau is set for OCP-
994 induced quenching of PBS excessive energy – and this, regardless of irradiance levels. We also show
995 that the first large-scale conformational changes occurring in photoactivated OCP take place on the
996 μs time scale, likely corresponding to the $P_{2'}$-P_3 transition. We note that ours is the first study to offer
997 time-resolved structural insights into the OCP photocycle with a non-resonant structural technique,
998 and as well the first TR structural study to be carried out on a protein with such a low quantum yield.
999 We hope our work attracts the attention of structural biologists on the possibilities offered by time-
1000 resolved SAXS/(WAXS).

1001

1002

1003

1004 **References**

1005 1. Agusti, S., S. Enriquez, H. Frost-Christensen, K. Sand-Jensen, and C.M. Duarte. 1994. Light
1006 Harvesting Among Photosynthetic Organisms. *Functional Ecology*. 8:273.

1007 2. Adir, N. 2005. Elucidation of the molecular structures of components of the phycobilisome:
1008 reconstructing a giant. *Photosynth. Res.* 85:15–32.

1009 3. Grossman, A.R., M.R. Schaefer, G.G. Chiang, and J.L. Collier. 1993. The phycobilisome, a light-
1010 harvesting complex responsive to environmental conditions. *Microbiol. Rev.* 57:725–749.

1011 4. Wilson, A., G. Ajlani, J.-M. Verbavatz, I. Vass, C.A. Kerfeld, and D. Kirilovsky. 2006. A soluble
1012 carotenoid protein involved in phycobilisome-related energy dissipation in cyanobacteria. *Plant*
1013 *Cell*. 18:992–1007.

1014 5. Wilson, A., C. Punginelli, A. Gall, C. Bonetti, M. Alexandre, J.-M. Routaboul, C.A. Kerfeld, R. van
1015 Grondelle, B. Robert, J.T.M. Kennis, and D. Kirilovsky. 2008. A photoactive carotenoid protein
1016 acting as light intensity sensor. *Proc. Natl. Acad. Sci. U. S. A.* 105:12075–12080.

1017 6. Demmig-Adams, B., G. Garab, W.A. Iii, and Govindjee. 2014. Non-Photochemical Quenching
1018 and Energy Dissipation in Plants, Algae and Cyanobacteria. Springer.

1019 7. Scott, M., C. McCollum, S. Vasil'ev, C. Crozier, G.S. Espie, M. Krol, N.P.A. Huner, and D. Bruce.
1020 2006. Mechanism of the down regulation of photosynthesis by blue light in the Cyanobacterium
1021 synechocystis sp. PCC 6803. *Biochemistry*. 45:8952–8958.

1022 8. Gwizdala, M., A. Wilson, and D. Kirilovsky. 2011. In vitro reconstitution of the cyanobacterial
1023 photoprotective mechanism mediated by the Orange Carotenoid Protein in Synechocystis PCC
1024 6803. *Plant Cell*. 23:2631–2643.

1025 9. Muzzopappa, F., and D. Kirilovsky. 2020. Changing Color for Photoprotection: The Orange
1026 Carotenoid Protein. *Trends Plant Sci.* 25:92–104.

1027 10. Muzzopappa, F., A. Wilson, and D. Kirilovsky. 2019. Interdomain interactions reveal the
1028 molecular evolution of the orange carotenoid protein. *Nat Plants*. 5:1076–1086.

1029 11. Kirilovsky, D., and C.A. Kerfeld. 2013. The Orange Carotenoid Protein: a blue-green light
1030 photoactive protein. *Photochem. Photobiol. Sci.* 12:1135–1143.

1031 12. Tian, L., I.H.M. van Stokkum, R.B.M. Koehorst, A. Jongerius, D. Kirilovsky, and H. van
1032 Amerongen. 2011. Site, rate, and mechanism of photoprotective quenching in cyanobacteria. *J.*
1033 *Am. Chem. Soc.* 133:18304–18311.

1034 13. Maksimov, E.G., N.N. Sluchanko, Y.B. Slonimskiy, E.A. Slutskaya, A.V. Stepanov, A.M.
1035 Argentova-Stevens, E.A. Shirshin, G.V. Tsoraev, K.E. Klementiev, O.V. Slatinskaya, E.P.
1036 Lukashev, T. Friedrich, V.Z. Paschenko, and A.B. Rubin. 2017. The photocycle of orange
1037 carotenoid protein conceals distinct intermediates and asynchronous changes in the carotenoid
1038 and protein components. *Sci. Rep.* 7:15548.

1039 14. Kerfeld, C.A., M.R. Sawaya, V. Brahmandam, D. Cascio, K.K. Ho, C.C. Trevithick-Sutton, D.W.
1040 Krogmann, and T.O. Yeates. 2003. The crystal structure of a cyanobacterial water-soluble
1041 carotenoid binding protein. *Structure*. 11:55–65.

15. Sedoud, A., R. López-Igual, A. Ur Rehman, A. Wilson, F. Perreau, C. Boulay, I. Vass, A. Krieger-Liszkay, and D. Kirilovsky. 2014. The Cyanobacterial Photoactive Orange Carotenoid Protein Is an Excellent Singlet Oxygen Quencher. *Plant Cell*. 26:1781–1791.

16. Bao, H., M.R. Melnicki, E.G. Pawlowski, M. Sutter, M. Agostoni, S. Lechno-Yossef, F. Cai, B.L. Montgomery, and C.A. Kerfeld. 2017. Additional families of orange carotenoid proteins in the photoprotective system of cyanobacteria. *Nat Plants*. 3:17089.

17. Wilson, A., J.N. Kinney, P.H. Zwart, C. Punginelli, S. D'Haene, F. Perreau, M.G. Klein, D. Kirilovsky, and C.A. Kerfeld. 2010. Structural determinants underlying photoprotection in the photoactive orange carotenoid protein of cyanobacteria. *J. Biol. Chem.* 285:18364–18375.

18. Leverenz, R.L., M. Sutter, A. Wilson, S. Gupta, A. Thurotte, C. Bourcier de Carbon, C.J. Petzold, C. Ralston, F. Perreau, D. Kirilovsky, and C.A. Kerfeld. 2015. PHOTOSYNTHESIS. A 12 Å carotenoid translocation in a photoswitch associated with cyanobacterial photoprotection. *Science*. 348:1463–1466.

19. Leverenz, R.L., D. Jallet, M.-D. Li, R.A. Mathies, D. Kirilovsky, and C.A. Kerfeld. 2014. Structural and functional modularity of the orange carotenoid protein: distinct roles for the N- and C-terminal domains in cyanobacterial photoprotection. *Plant Cell*. 26:426–437.

20. Lu, Y., H. Liu, R.G. Saer, H. Zhang, C.M. Meyer, V.L. Li, L. Shi, J.D. King, M.L. Gross, and R.E. Blankenship. 2017. Native Mass Spectrometry Analysis of Oligomerization States of Fluorescence Recovery Protein and Orange Carotenoid Protein: Two Proteins Involved in the Cyanobacterial Photoprotection Cycle. *Biochemistry*. 56:160–166.

21. Golub, M., M. Moldenhauer, F.-J. Schmitt, A. Feoktystov, H. Mändar, E. Maksimov, T. Friedrich, and J. Pieper. 2019. Solution Structure and Conformational Flexibility in the Active State of the Orange Carotenoid Protein: Part I. Small-Angle Scattering. *J. Phys. Chem. B*. 123:9525–9535.

22. Golub, M., M. Moldenhauer, F.-J. Schmitt, W. Lohstroh, E.G. Maksimov, T. Friedrich, and J. Pieper. 2019. Solution Structure and Conformational Flexibility in the Active State of the Orange Carotenoid Protein. Part II: Quasielastic Neutron Scattering. *J. Phys. Chem. B*. 123:9536–9545.

23. Liu, H., H. Zhang, G.S. Orf, Y. Lu, J. Jiang, J.D. King, N.R. Wolf, M.L. Gross, and R.E. Blankenship. 2016. Dramatic Domain Rearrangements of the Cyanobacterial Orange Carotenoid Protein upon Photoactivation. *Biochemistry*. 55:1003–1009.

24. Zhang, H., H. Liu, Y. Lu, N.R. Wolf, M.L. Gross, and R.E. Blankenship. 2016. Native mass spectrometry and ion mobility characterize the orange carotenoid protein functional domains. *Biochim. Biophys. Acta*. 1857:734–739.

25. Konold, P.E., I.H.M. van Stokkum, F. Muzzopappa, A. Wilson, M.-L. Groot, D. Kirilovsky, and J.T.M. Kennis. 2019. Photoactivation Mechanism, Timing of Protein Secondary Structure Dynamics and Carotenoid Translocation in the Orange Carotenoid Protein. *J. Am. Chem. Soc.* 141:520–530.

26. Mezzetti, A., M. Alexandre, A. Thurotte, A. Wilson, M. Gwizdala, and D. Kirilovsky. 2019. Two-Step Structural Changes in Orange Carotenoid Protein Photoactivation Revealed by Time-Resolved Fourier Transform Infrared Spectroscopy. *J. Phys. Chem. B*. 123:3259–3266.

27. Maksimov, E.G., E.A. Protasova, G.V. Tsoraev, I.A. Yaroshevich, A.I. Maydykovskiy, E.A. Shirshin, T.S. Gostev, A. Jelzow, M. Moldenhauer, Y.B. Slonimskiy, N.N. Sluchanko, and T.

1083 Friedrich. 2020. Probing of carotenoid-tryptophan hydrogen bonding dynamics in the single-
1084 tryptophan photoactive Orange Carotenoid Protein. *Sci. Rep.* 10:11729.

1085 28. Gupta, S., M. Guttman, R.L. Leverenz, K. Zhumadilova, E.G. Pawlowski, C.J. Petzold, K.K. Lee,
1086 C.Y. Ralston, and C.A. Kerfeld. 2015. Local and global structural drivers for the photoactivation
1087 of the orange carotenoid protein. *Proc. Natl. Acad. Sci. U. S. A.* 112:E5567-74.

1088 29. Gupta, S., M. Sutter, S.G. Remesh, M.A. Dominguez-Martin, H. Bao, X.A. Feng, L.-J.G. Chan,
1089 C.J. Petzold, C.A. Kerfeld, and C.Y. Ralston. 2019. X-ray radiolytic labeling reveals the molecular
1090 basis of orange carotenoid protein photoprotection and its interactions with fluorescence
1091 recovery protein. *J. Biol. Chem.* 294:8848–8860.

1092 30. Bandara, S., Z. Ren, L. Lu, X. Zeng, H. Shin, K.-H. Zhao, and X. Yang. 2017. Photoactivation
1093 mechanism of a carotenoid-based photoreceptor. *Proc. Natl. Acad. Sci. U. S. A.* 114:6286–6291.

1094 31. Bourcier de Carbon, C., A. Thurotte, A. Wilson, F. Perreau, and D. Kirilovsky. 2015. Biosynthesis
1095 of soluble carotenoid holoproteins in Escherichia coli. *Sci. Rep.* 5:9085.

1096 32. Sluchanko, N.N., K.E. Klementiev, E.A. Shirshin, G.V. Tsoraev, T. Friedrich, and E.G. Maksimov.
1097 2017. The purple Trp288Ala mutant of Synechocystis OCP persistently quenches phycobilisome
1098 fluorescence and tightly interacts with FRP. *Biochim. Biophys. Acta Bioenerg.* 1858:1–11.

1099 33. Gasteiger, E., C. Hoogland, A. Gattiker, S. Duvaud, M.R. Wilkins, R.D. Appel, and A. Bairoch.
1100 2005. Protein Identification and Analysis Tools on the ExPASy Server. *The Proteomics Protocols*
1101 *Handbook*. 571–607.

1102 34. Walker, J.M. 2005. The Proteomics Protocols Handbook. Springer Science & Business Media.

1103 35. Svergun, D.I. 1992. Determination of the regularization parameter in indirect-transform methods
1104 using perceptual criteria. *J. Appl. Crystallogr.* 25:495–503.

1105 36. Franke, D., M.V. Petoukhov, P.V. Konarev, A. Panjkovich, A. Tuukkanen, H.D.T. Mertens, A.G.
1106 Kikhney, N.R. Hajizadeh, J.M. Franklin, C.M. Jeffries, and D.I. Svergun. 2017. : a comprehensive
1107 data analysis suite for small-angle scattering from macromolecular solutions. *J. Appl. Crystallogr.*
1108 50:1212–1225.

1109 37. Franke, D., and D.I. Svergun. 2009. , a program for rapid shape determination in small-angle
1110 scattering. *J. Appl. Crystallogr.* 42:342–346.

1111 38. Konarev, P.V., V.V. Volkov, A.V. Sokolova, M.H.J. Koch, and D.I. Svergun. 2003. PRIMUS: a
1112 Windows PC-based system for small-angle scattering data analysis. *J. Appl. Crystallogr.*
1113 36:1277–1282.

1114 39. Melnicki, M.R., R.L. Leverenz, M. Sutter, R. López-Igual, A. Wilson, E.G. Pawlowski, F. Perreau,
1115 D. Kirilovsky, and C.A. Kerfeld. 2016. Structure, Diversity, and Evolution of a New Family of
1116 Soluble Carotenoid-Binding Proteins in Cyanobacteria. *Mol. Plant*. 9:1379–1394.

1117 40. Dominguez-Martin, M.A., T. Polívka, M. Sutter, B. Ferlez, S. Lechno-Yossef, B.L. Montgomery,
1118 and C.A. Kerfeld. 2019. Structural and spectroscopic characterization of HCP2. *Biochim.*
1119 *Biophys. Acta Bioenerg.* 1860:414–424.

41. Harris, D., A. Wilson, F. Muzzopappa, N.N. Sluchanko, T. Friedrich, E.G. Maksimov, D. Kirilovsky, and N. Adir. 2018. Structural rearrangements in the C-terminal domain homolog of Orange Carotenoid Protein are crucial for carotenoid transfer. *Commun Biol*. 1:125.

42. Newville, M., T. Stensitzki, D.B. Allen, and A. Ingargiola. 2014. LMFIT: Non-Linear Least-Square Minimization and Curve-Fitting for Python. .

43. Burdzinski, G., M. Bayda, G.L. Hug, M. Majchrzak, B. Marciniec, and B. Marciniak. 2011. Time-resolved studies on the photoisomerization of a phenylene–silylene–vinylene type compound in its first singlet excited state. *Journal of Luminescence*. 131:577–580.

44. Müller, P., and K. Brettel. 2012. [Ru(bpy)(3)](2+) as a reference in transient absorption spectroscopy: differential absorption coefficients for formation of the long-lived (3)MLCT excited state. *Photochem. Photobiol. Sci.* 11:632–636.

45. Cammarata, M., M. Levantino, F. Schotte, P.A. Anfinrud, F. Ewald, J. Choi, A. Cupane, M. Wulff, and H. Ihee. 2008. Tracking the structural dynamics of proteins in solution using time-resolved wide-angle X-ray scattering. *Nat. Methods*. 5:881–886.

46. Cammarata, M., M. Levantino, M. Wulff, and A. Cupane. 2010. Unveiling the timescale of the R-T transition in human hemoglobin. *J. Mol. Biol.* 400:951–962.

47. Henry, E.R., and J. Hofrichter. 1992. [8] Singular value decomposition: Application to analysis of experimental data. In: Methods in Enzymology. Academic Press. pp. 129–192.

48. Svergun, D.I. 1999. Restoring low resolution structure of biological macromolecules from solution scattering using simulated annealing. *Biophys. J.* 76:2879–2886.

49. Piiadov, V., E.A. de Araújo, M.O. Neto, A.F. Craievich, and I. Polikarpov. 2019. SAXSMoW 2.0: Online calculator of the molecular weight of proteins in dilute solution from experimental SAXS data measured on a relative scale. *Protein Science*. 28:454–463.

50. Wilson, A., M. Gwizdala, A. Mezzetti, M. Alexandre, C.A. Kerfeld, and D. Kirilovsky. 2012. The essential role of the N-terminal domain of the orange carotenoid protein in cyanobacterial photoprotection: importance of a positive charge for phycobilisome binding. *Plant Cell*. 24:1972–1983.

51. Moldenhauer, M., N.N. Sluchanko, D. Buhrke, D.V. Zlenko, N.N. Tavraz, F.-J. Schmitt, P. Hildebrandt, E.G. Maksimov, and T. Friedrich. 2017. Assembly of photoactive orange carotenoid protein from its domains unravels a carotenoid shuttle mechanism. *Photosynth. Res.* 133:327–341.

52. Muzzopappa, F., A. Wilson, V. Yogarajah, S. Cot, F. Perreau, C. Montigny, C. Bourcier de Carbon, and D. Kirilovsky. 2017. Paralogs of the C-Terminal Domain of the Cyanobacterial Orange Carotenoid Protein Are Carotenoid Donors to Helical Carotenoid Proteins. *Plant Physiol.* 175:1283–1303.

53. Yaroshevich, I.A., E.G. Maksimov, N.N. Sluchanko, D.V. Zlenko, A.V. Stepanov, E.A. Slutskaya, Y.B. Slonimskiy, V.S. Botnarevskii, A. Remeeva, I. Gushchin, K. Kovalev, V.I. Gordeliy, I.V. Shelaev, F.E. Gostev, D. Khakhulin, V.V. Poddubnyy, T.S. Gostev, D.A. Cherepanov, T. Polívka, M. Kloz, T. Friedrich, V.Z. Paschenko, V.A. Nadtochenko, A.B. Rubin, and M.P. Kirpichnikov. 2021. Role of hydrogen bond alternation and charge transfer states in photoactivation of the Orange Carotenoid Protein. *Commun Biol*. 4:539.

1161 54. Zhang, H., H. Liu, D.M. Niedzwiedzki, M. Prado, J. Jiang, M.L. Gross, and R.E. Blankenship.
1162 2014. Molecular mechanism of photoactivation and structural location of the cyanobacterial
1163 orange carotenoid protein. *Biochemistry*. 53:13–19.

1164 55. Maksimov, E.G., E.A. Shirshin, N.N. Sluchanko, D.V. Zlenko, E.Y. Parshina, G.V. Tsoraev, K.E.
1165 Klementiev, G.S. Budylin, F.-J. Schmitt, T. Friedrich, V.V. Fadeev, V.Z. Paschenko, and A.B.
1166 Rubin. 2015. The Signaling State of Orange Carotenoid Protein. *Biophys. J.* 109:595–607.

1167 56. Balevičius, V., Jr, D. Abramavicius, T. Polívka, A. Galestian Pour, and J. Hauer. 2016. A
1168 Unified Picture of S* in Carotenoids. *J. Phys. Chem. Lett.* 7:3347–3352.

1169

Author Contributions: J.-P.C. coordinated the project. E.A.A., G.S. and A.T. performed static X-ray scattering. E.A.A. analyzed static X-ray scattering data and performed thermal recovery assays. S.N., M.S. and G.B. performed time-resolved spectroscopy. S.N. analyzed time-resolved spectroscopy data. A.W. and D.K. performed protein expression and purification; E.A.A., N.Z. and R.M. prepared protein samples. E.D.Z. performed fitting analysis of thermal recovery data. J.-P.C., G.S. and M.L. designed the TR-SAXS experiment. E.A.A., S.N., M.L., F.M., G.B., M.S., G.S., J.-P.C. performed the TR-SAXS experiment. G.S. analyzed time-resolved X-ray scattering data; E.A.A. and J.-P.C. wrote the paper with input from other coauthors.

Acknowledgments: We are grateful to Ilme Schlichting and Martin Weik for continued support of the project. We thank the SOLEIL and ESRF synchrotron radiation facilities for repeated allocation of beamtime on the SWING and ID09 beamlines, where the static and time-resolved SAXS experiments were performed, respectively. IBS acknowledges integration into the Interdisciplinary Research Institute of Grenoble (IRIG, CEA). This work was supported by the Agence Nationale de la Recherche (grants ANR-17-CE11-0018-01 and ANR-2018-CE11-0005-02 to J.-P.C.) and the Polish National Science Centre (NCN project 2018/31/N/ST4/03983), and used the platforms of the Grenoble Instruct-ERIC center (ISBG; UMS 3518 CNRS-CEA-UGA-EMBL) within the Grenoble Partnership for Structural Biology (PSB). Platform access was supported by FRISBI (ANR-10-INBS-05-02) and GRAL, a project of the University Grenoble Alpes graduate school (Ecoles Universitaires de Recherche) CBH-EUR-GS (ANR-17-EURE-0003). The access and travel fees of G.B. and S.N. to ESRF were financed by the Polish Ministry of Science and High Education - decision number: DIR/WK/2016/19. R.M. is supported by a GRAL PhD. Fellowship (7C047GRAL).

Competing interests: Authors declare no competing interests.

Data and materials availability: All data are available in the main text or the supplementary materials. Raw SAXS data can be made available upon request.

1197 **Figures captions (1688 words)**

1198 **FIGURE 1. OCP crystallize as a dimer.** (*A, B*) Structure of the dark-adapted *Synechocystis* PCC
1199 6703 OCP^O dimer (PDB id: 3MG1). The dimerization interface is supported by conserved H-bonds
1200 between facing D19, R27, N134 (shown as sticks). Within the dimer, each OCP monomer features
1201 two domains: (i) an N-terminal domain (NTD; coloured in shades of orange) comprising residues 1–
1202 165; (ii) a C-terminal domain (CTD; coloured in shades of grey) comprising residues 193–317. The
1203 two domains are attached by a ~ 20 residue linker (coloured in shades of cyan). The keto-carotenoid
1204 pigment, ECN (coloured in slate) binds in a ~ 35 Å long hydrophobic tunnel spanning the two domains.
1205 In the CTD, ECN establishes two H-bonds with Y201 and W288. The N-terminal extension (NTE) and
1206 the C-terminal tail (CTT) are shown in pink and black, respectively.

1207 **FIGURE 2. Static X-ray scattering reveals changes in the OCP structure as a function of**
1208 **concentration and upon illumination.** (*A, B)* X-ray scattering patterns of (*A*) dark-adapted OCP^O_{wt-}
1209 $_{Ctag}$ and (*B*) $OCP^O_{R27L-Ntag}$ at various concentrations. The insets show overlays of the low-resolution
1210 data in the Guinier region. their corresponding overlays in the Guinier region (insets) at various
1211 concentrations. *(C)* Pair distance distribution function P(r) of dark-adapted $OCP^O_{wt-Ctag}$ and OCP^O_{R27L-}
1212 $_{Ntag}$ at increasing concentrations. (*D, E, F*) X-ray scattering patterns of (*D*) light-adapted $OCP^R_{wt-Ctag}$
1213 and (*E*) $OCP^R_{R27L-Ntag}$, and (*F*) pair distance distribution function P(r) of light-adapted of $OCP^R_{wt-Ctag}$
1214 and $OCP^R_{R27L-Ntag}$ at increasing concentrations.

1215 **FIGURE 3. Probing OCP oligomerization in dark and light-adapted states.** (*A*) Evolution of the
1216 radii of gyration (Rg) of dark-adapted and light-adapted $OCP_{wt-Ctag}$ and $OCP_{R27L-Ntag}$ as a function of
1217 concentration. Error bars: standard deviation. (*B*) Estimation of the oligomerization state of OCP^O_{wt-}
1218 $_{Ctag}$ as a function of concentration. (*C*) Light minus dark SAXS difference patterns ($\Delta S(q)$) for OCP_{R27L}
1219 $_{Ntag}$ at 10.5 mg/ml and $OCP_{wt-Ctag}$ at 10.5 mg/ml (signal recorded on the bio-SAXS SWING beamline,
1220 Synchrotron SOLEIL) and 23 mg/ml (signal recorder at ID09 beamline, ESRF). (*D*, *E*, *F*) Plots of the
1221 retained pre-exponential factors retrieved from fits of recovery data as a function of concentration. (*D*)
1222 $OCP_{R27L-Ntag}$, (*E*) $OCP_{wt-Ntag}$ and (*F*) $OCP_{wt-Ctag}$. The $OCP_{R27L-Ntag}$ and $OCP_{wt-Ntag}$ data are best fit by a
1223 model accounting for three exponential components, whereas the $OCP_{wt-Ctag}$ data require inclusion of
1224 a fourth exponential component. Fitting parameters are reported in Table S2 and S3.

1225 **FIGURE 4. Molecular envelopes and models fitted thereof for dark-adapted and light-adapted**
1226 **$OCP_{wt-Ctag}$ and $OCP_{R27L-Ntag}$ at increasing concentrations.** The molecular envelopes, determined
1227 based on experimental static SAXS data are shown for $OCP_{R27L-Ntag}$ and $OCP_{wt-Ctag}$ in their dark-
1228 adapted and light-adapted states at three concentrations. The proposed models are overlayed on the
1229 molecular envelopes. For the dark-adapted $OCP_{R27L-Ntag}$, the molecular envelopes are consistent with
1230 the presence of an OCP^O monomer, whereas for the dark-adapted $OCP_{wt-Ctag}$, the molecular

1231 envelopes are better fitted by the crystallographic OCP^O dimer (PDB id: 3MG1). At each
1232 concentration, the molecular envelopes determined for light-adapted $OCP_{R27L\text{-}Ntag}$ and $OCP_{wt\text{-}Ctag}$ are
1233 similar, and consistent with the presence of an OCP^R dimer, at 0.7 and 3.5 mg/ml, and an OCP^R
1234 tetramer, at 10.5 mg/ml.

1235 **FIGURE 5. Transient absorption spectroscopy enables identification of three intermediate**
1236 **states on the 50 ns – 0.5 s time scale. The figure shows the time evolution of the difference**
1237 absorption signal at 565 nm. (*A*) Nanosecond transient absorption data for $OCP_{wt\text{-}Ctag}$, $OCP_{wt\text{-}Ntag}$ and
1238 $OCP_{R27L\text{-}Ntag}$ at 12 μM. (*B*) Nanosecond transient absorption data for $OCP_{R27L\text{-}Ntag}$ at 12 μM and various
1239 temperatures. (*C* and *D*) Comparison of nanosecond transient absorption data between $OCP_{wt\text{-}Ctag}$
1240 and $OCP_{R27L\text{-}Ntag}$ at 50 μM, and $OCP_{wt\text{-}Ctag}$ and $OCP_{R27L\text{-}Ntag}$ at 250 μM, respectively. (*E-F*) Eyring plots
1241 used to extract enthalpy and entropy of activation for $OCP_{wt\text{-}Ctag}$ (*E*) and $OCP_{R27L\text{-}Ntag}$ (*F*), ($\kappa = 1$ is
1242 assumed). See Figure S7 for complementary data.

1243 **FIGURE 6. Time-resolved X-ray scattering reveals the kinetics of light-induced structural**
1244 **changes in the μs-ms time scale.** (*A*) Comparison of the time resolved laser-on - laser-off X-ray
1245 difference pattern obtained 1 ms after excitation by either a 5 ns pulse at 430 nm or a 450 ns pulse
1246 at 527 nm. The static OCP^R - OCP^O X-ray difference pattern, calculated by subtracting the pattern of
1247 the dark-adapted sample from that of the continuously-illuminated sample (430 nm) and scaled by a
1248 factor 0.018, is shown for comparison. (*B*) Integrated difference scattering in the region $0 < q < 0.15$
1249 $Å^{-1}$ as a function of the number of laser pulses (527 nm) for $OCP_{wt\text{-}Ctag}$ (blue circles) and $OCP_{wt\text{-}Ntag}$
1250 (red squares). Pulse energy and duration were 2 mJ and 400 ns, respectively, and the pulses were
1251 spaced by 1 ms. (*C*) Light-induced time-resolved X-ray scattering difference patterns for $OCP_{wt\text{-}Ctag}$.
1252 The static OCP^R - OCP^O X-ray scattering difference pattern (scaled by a factor 0.018) is also shown
1253 for comparison. Data is vertically offset for clarity. (*D*) Time evolution of the integrated difference
1254 scattering in the region $0 < q < 0.15$ $Å^{-1}$ after laser excitation at 527 nm for $OCP_{wt\text{-}Ctag}$ (blue and green
1255 circles) and $OCP_{wt\text{-}Ntag}$ (red squares). Dashed lines are fitting curves with a double exponential
1256 function. Specific to the $OCP_{wt\text{-}Ctag}$ sample, the blue and green circles indicate patterns collected with
1257 either one or multiples pulses.

1258 **FIGURE 7. OCP photoactivation and recovery are limited by oligomerization processes.** OCP
1259 monomers and dimers are represented schematically with their N-terminal (coloured in orange and
1260 red for OCP^O and OCP^R, respectively) and C-terminal domains (coloured in white) represented by
1261 two circles. The ground state keto-carotenoid is shown in grey. Ticks and crosses in the CTD
1262 respectively indicate presence and absence of H-bonds between the carotenoid and CTD residues
1263 Tyr201 and Trp288. The presence of ticks in the NTD indicate closure of the carotenoid tunnel at its
1264 NTD end and presence of π-stacking interactions between the carotenoid and NTD residues Tyr44

1265 and Trp110. Our data show that dark-adapted OCP_{wt} forms dimers, with a dissociation constant of ~
1266 14 μM. The dimerization interface at play is likely that which has been repeatedly observed in the
1267 OCP crystal structures, since substitution for a leucine (L) of R27, involved in a conserved salt-bridge
1268 to D19 at this interface, fully abrogates dimerization. In the event where only one of the two monomers
1269 in a dimer is activated, it may undergo all photoactivation steps until formation of P_3, but will promptly
1270 revert to the dark state unless the second monomer is as well photoactivated (OCP^O/OCP^R). Indeed,
1271 domain dissociation may occur after dimer disassembly, which itself can only occur after NTE
1272 detachment, but the latter depends on the carotenoid achieving a successful transit across the NTD,
1273 *i.e.,* formation of P_3. In practice, this means that reaching the OCP^R state in a pulsed illumination
1274 experiment probing OCP_{wt} dimers is extremely unlikely unless re-excitation can be achieved within
1275 the lapse of the excitation pulse. Indeed, the probability that two monomers in a dimer can be activated
1276 by the same pulse is ~ $1e^{-5}$. Nonetheless, under continuous illumination, the OCP^R state can be
1277 accumulated, which first coalesces into dimers, with a dissociation constant similar to that displayed
1278 by dark-adapted OCP (~ 14 μM), but may as well form tetramers, with a nearly 20 times higher
1279 dissociation constant (~ 286 μM). Existence of these oligomers elevate the overall energy barrier for
1280 a full recovery of the starting dark OCP^O to occur, and therefore delay the upturn of the OCP^O state,
1281 as each OCP^R oligomer presents a different lifetime. It is yet the reassociation of dark monomers into
1282 dimers that constitute the limiting step in the recovery.

1283 **FIGURE 8. Proposed model for OCP photoactivation and recovery upon pulsed excitation.**
1284 OCP is schematically represented with its N-terminal (coloured in orange for OCP^O, pink for P_1,
1285 magenta for P_2, red for P_2', P_3, OCP^R, Int.1, Int.2 and Int.3) and C-terminal domains (coloured in white),
1286 represented by two circles. The ground state keto-carotenoid is shown in grey. Ticks and crosses in
1287 the CTD respectively indicate presence and absence of H-bonds between the carotenoid and CTD
1288 residues Tyr201 and Trp288. Ticks and crosses in the NTD respectively indicate presence and
1289 absence of π-stacking interactions between the carotenoid and NTD residues Tyr44 and Trp110. For
1290 clarity, only the OCP monomer is shown. Complete migration of the carotenoid across the NTD tunnel
1291 requires the unsettling of these interactions and passage of a bottleneck contributed by NTD residues
1292 Leu37, Met83 and Met117, further down the tunnel. We posit that upon photoexcitation, the
1293 carotenoid of OCP forms multiple excited states, only one of which is parent to the first photoproduct
1294 P_1. Non-productive photoexcitation yet does not allow recovery of a photo-excitable state; instead, a
1295 numbed state forms that displays all spectral characteristics of the ground state but cannot be
1296 reactivated before a time delay estimated to lie between 0.5 μs and 1 ms. We can only presume that
1297 before then, important residues for the photoactivation mechanism (*e.g.* Y44 and W110) have not
1298 returned to their ground state positions, despite the carotenoid being at its H-bonding position and
1299 the protein therefore displaying an orange spectrum. Productive photoexcitation yields P_1, after
1300 rupture of H-bonds to the carotenoid; past 50 ns, the carotenoid repositions at the NTD/CTD interface

(P_2), before bridging the above-mentioned bottleneck at 500 ns (P_2'). Conformational changes occur in the NTD domain, enabling the carotenoid to pass across the NTD wall and its β2 ionone ring to become solvent-exposed (P_3). At all steps before P_3, back-migration of the carotenoid to its dark-state position can occur with rapid recovery of the orange state, as the tunnel remains shielded from the bulk. After P_3, however, recovery follows another pathway that does not enable rapid recovery of the orange state spectrum. In the fraction of P_3 that does not recover, the NTE will eventually detach from the CTD β-sheet, however this step was not visible in our data. Either before or after detachment of the NTE, back-migration of the carotenoid can occur, with characteristic times of 1 and 50-200 ms, respectively. Separation of the two domains may yet take place before occurrence of carotenoid back-migration and NTE reattachment, yielding the minute-lived OCP^R state, after repositioning of the CTT over the empty CTD half of the carotenoid tunnel. P_3 could thus serve as an intermediate along the OCP^R to OCP^O recovery.

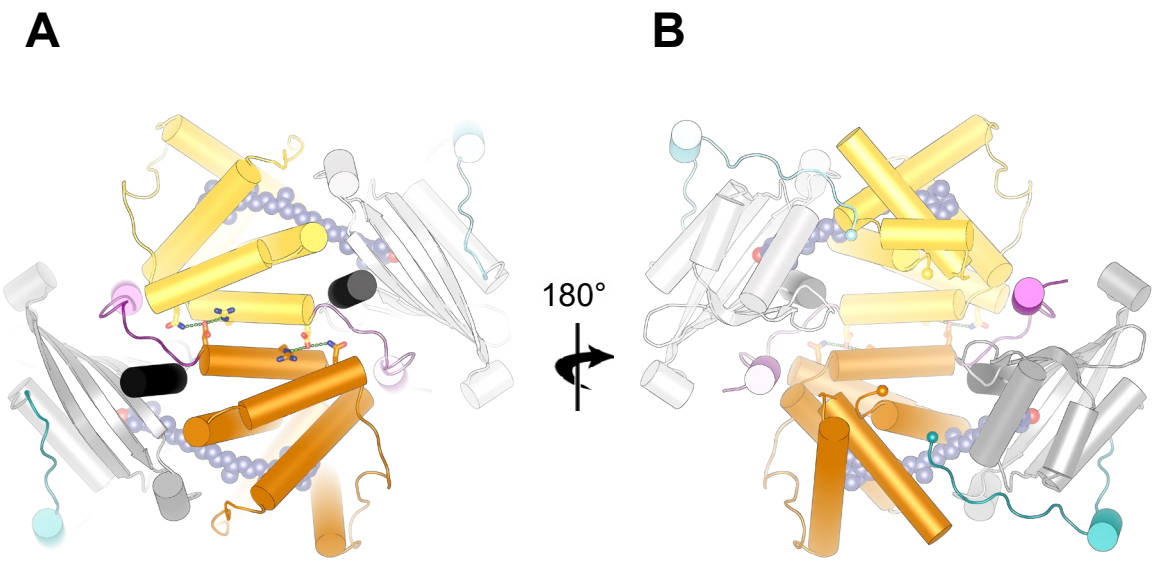

FIGURE 1. OCP crystallize as a dimer. (*A, B*) Structure of the dark-adapted *Synechocystis* PCC 6703 OCP^{O} dimer (PDB id: 3MG1). The dimerization interface is supported by conserved H-bonds between facing D19, R27, N134 (shown as sticks). Within the dimer, each OCP monomer features two domains: (i) an N-terminal domain (NTD; coloured in shades of orange) comprising residues 1–165; (ii) a C-terminal domain (CTD; coloured in shades of grey) comprising residues 193–317. The two domains are attached by a ~ 20 residue linker (coloured in shades of cyan). The keto-carotenoid pigment, ECN (coloured in slate) binds in a ~ 35 Å long hydrophobic tunnel spanning the two domains. In the CTD, ECN establishes two H-bonds with Y201 and W288. The N-terminal extension (NTE) and the C-terminal tail (CTT) are shown in pink and black, respectively.

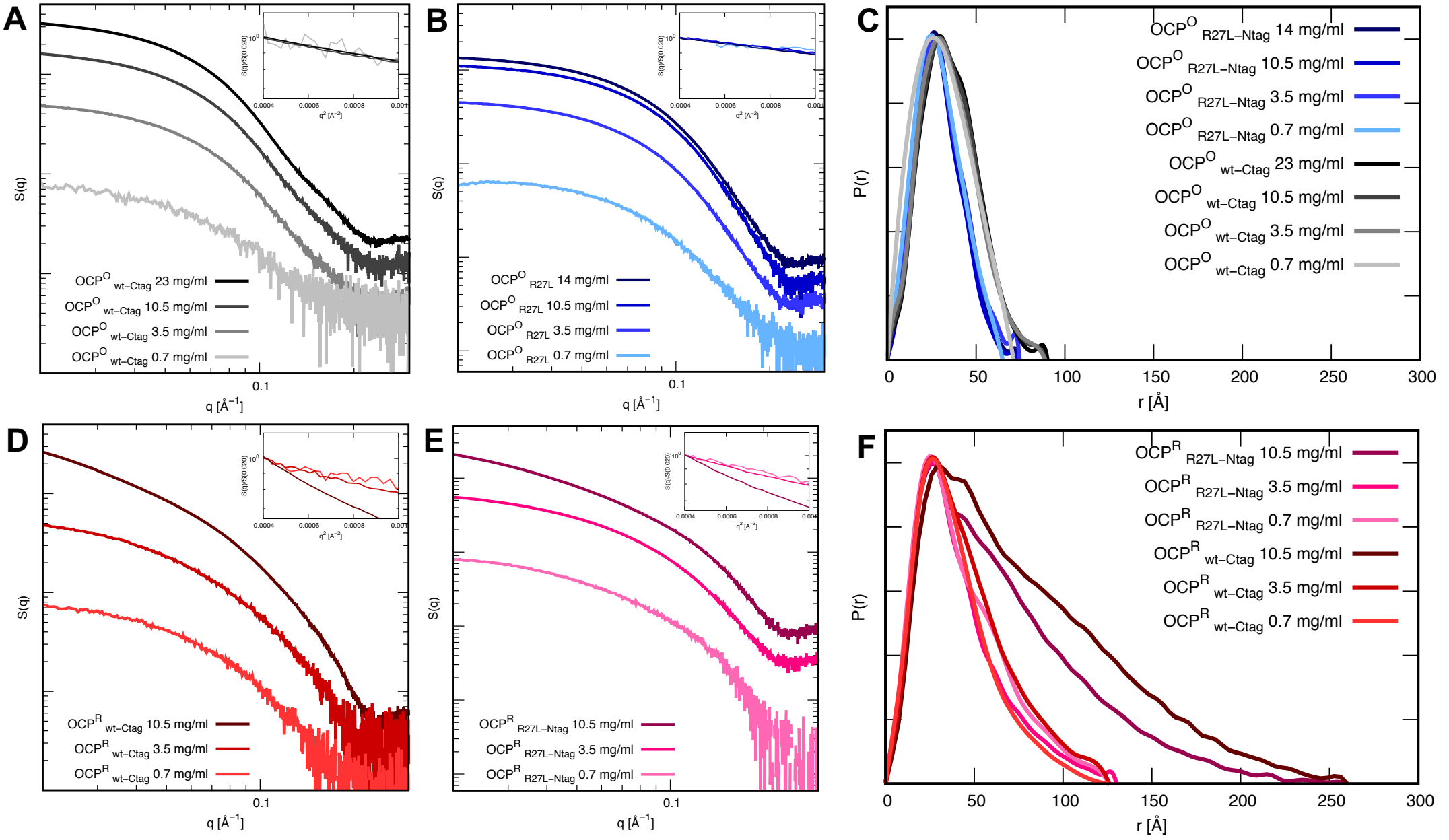

FIGURE 2. Static X-ray scattering reveals changes in the OCP structure as a function of concentration and upon illumination. (*A, B)* X-ray scattering patterns of (*A*) dark-adapted $OCP^{O}_{wt\text{-}Ctag}$ and (*B*) $OCP^{O}_{R27L\text{-}Ntag}$ at various concentrations. The insets show overlays of the low-resolution data in the Guinier region. their corresponding overlays in the Guinier region (insets) at various concentrations. *(C)* Pair distance distribution function P(r) of dark-adapted $OCP^{O}_{wt\text{-}Ctag}$ and $OCP^{O}_{R27L\text{-}Ntag}$ at increasing concentrations. (*D, E, F*) X-ray scattering patterns of (*D*) light-adapted $OCP^{R}_{wt\text{-}Ctag}$ and (*E*) $OCP^{R}_{R27L\text{-}Ntag}$, and (*F*) pair distance distribution function P(r) of light-adapted of $OCP^{R}_{wt\text{-}Ctag}$ and $OCP^{R}_{R27L\text{-}Ntag}$ at increasing concentrations.

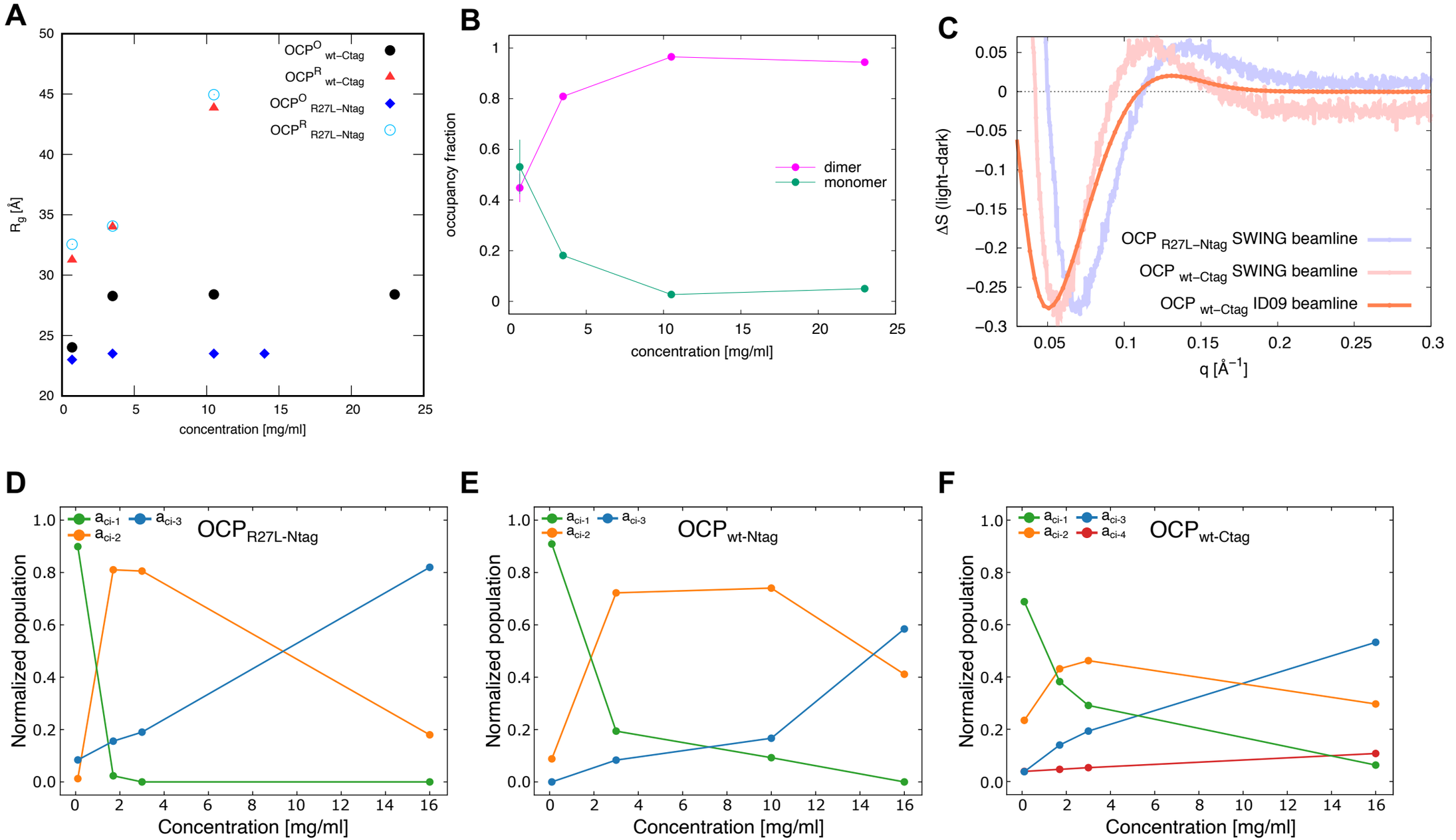

FIGURE 3. Probing OCP oligomerization in dark and light-adapted states. (*A*) Evolution of the radii of gyration (Rg) of dark-adapted and light-adapted $OCP_{wt-Ctag}$ and $OCP_{R27L-Ntag}$ as a function of concentration. Error bars: standard deviation. (*B*) Estimation of the oligomerization state of $OCP^O_{wt-Ctag}$ as a function of concentration. (*C*) Light minus dark SAXS difference patterns ($\Delta S(q)$) for $OCP_{R27L\ Ntag}$ at 10.5 mg/ml and $OCP_{wt-Ctag}$ at 10.5 mg/ml (signal recorded on the bio-SAXS SWING beamline, Synchrotron SOLEIL) and 23 mg/ml (signal recorder at ID09 beamline, ESRF). (*D*, *E*, *F*) Plots of the retained pre-exponential factors retrieved from fits of recovery data as a function of concentration. (*D*) $OCP_{R27L-Ntag}$, (*E*) $OCP_{wt-Ntag}$ and (*F*) $OCP_{wt-Ctag}$. The $OCP_{R27L-Ntag}$ and $OCP_{wt-Ntag}$ data are best fit by a model accounting for three exponential components, whereas the $OCP_{wt-Ctag}$ data require inclusion of a fourth exponential component. Fitting parameters are reported in Table S2 and S3.

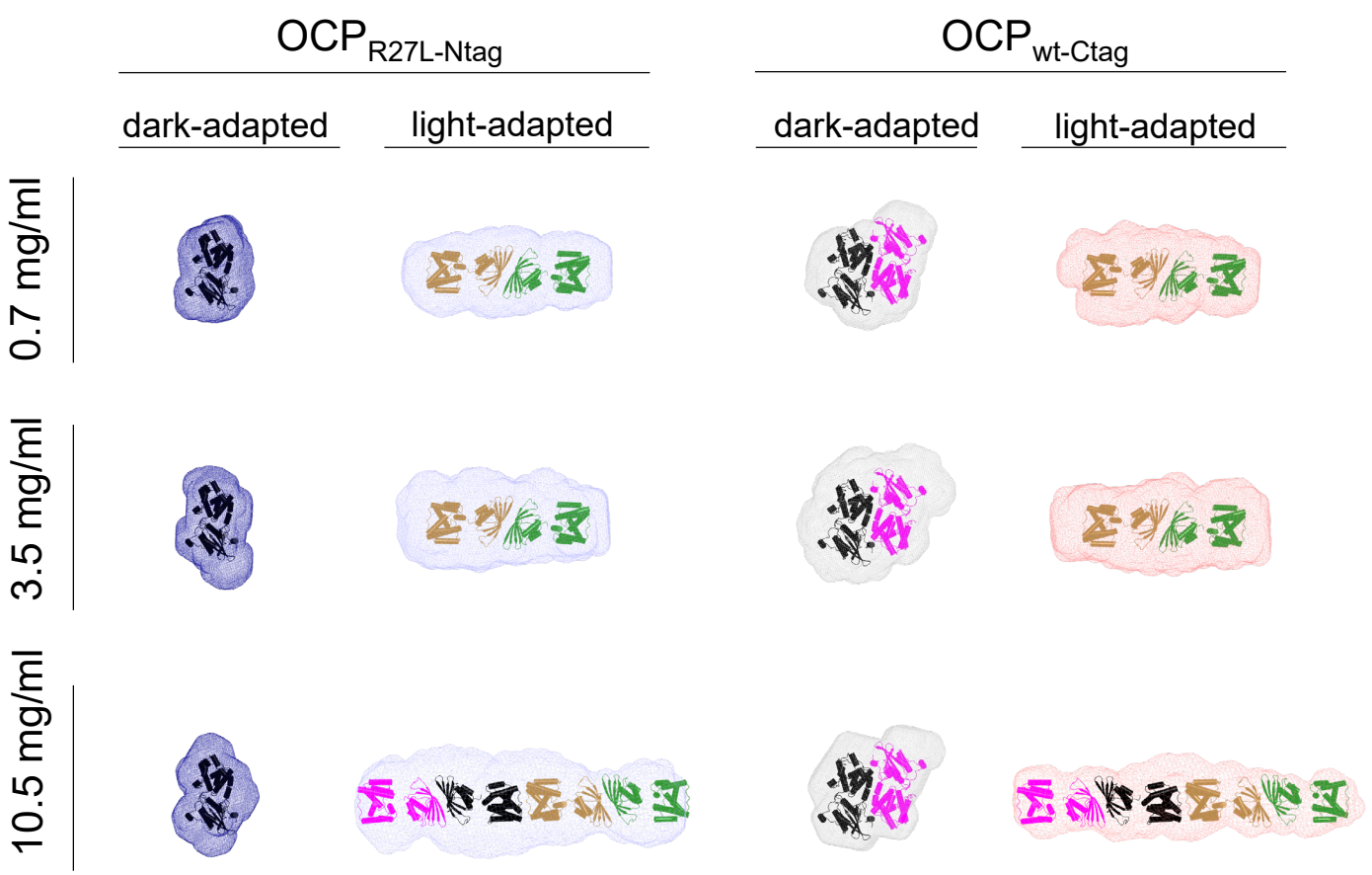

FIGURE 4. Molecular envelopes and models fitted thereof for dark-adapted and light-adapted $OCP_{wt\text{-}Ctag}$ and $OCP_{R27L\text{-}Ntag}$ at increasing concentrations. The molecular envelopes, determined based on experimental static SAXS data are shown for $OCP_{R27L\text{-}Ntag}$ and $OCP_{wt\text{-}Ctag}$ in their dark-adapted and light-adapted states at three concentrations. The proposed models are overlayed on the molecular envelopes. For the dark-adapted $OCP_{R27L\text{-}Ntag}$, the molecular envelopes are consistent with the presence of an OCP^{O} monomer, whereas for the dark-adapted $OCP_{wt\text{-}Ctag}$, the molecular envelopes are better fitted by the crystallographic OCP^{O} dimer (PDB id: 3MG1). At each concentration, the molecular envelopes determined for light-adapted $OCP_{R27L\text{-}Ntag}$ and $OCP_{wt\text{-}Ctag}$ are similar, and consistent with the presence of an OCP^{R} dimer, at 0.7 and 3.5 mg/ml, and an OCP^{R} tetramer, at 10.5 mg/ml.

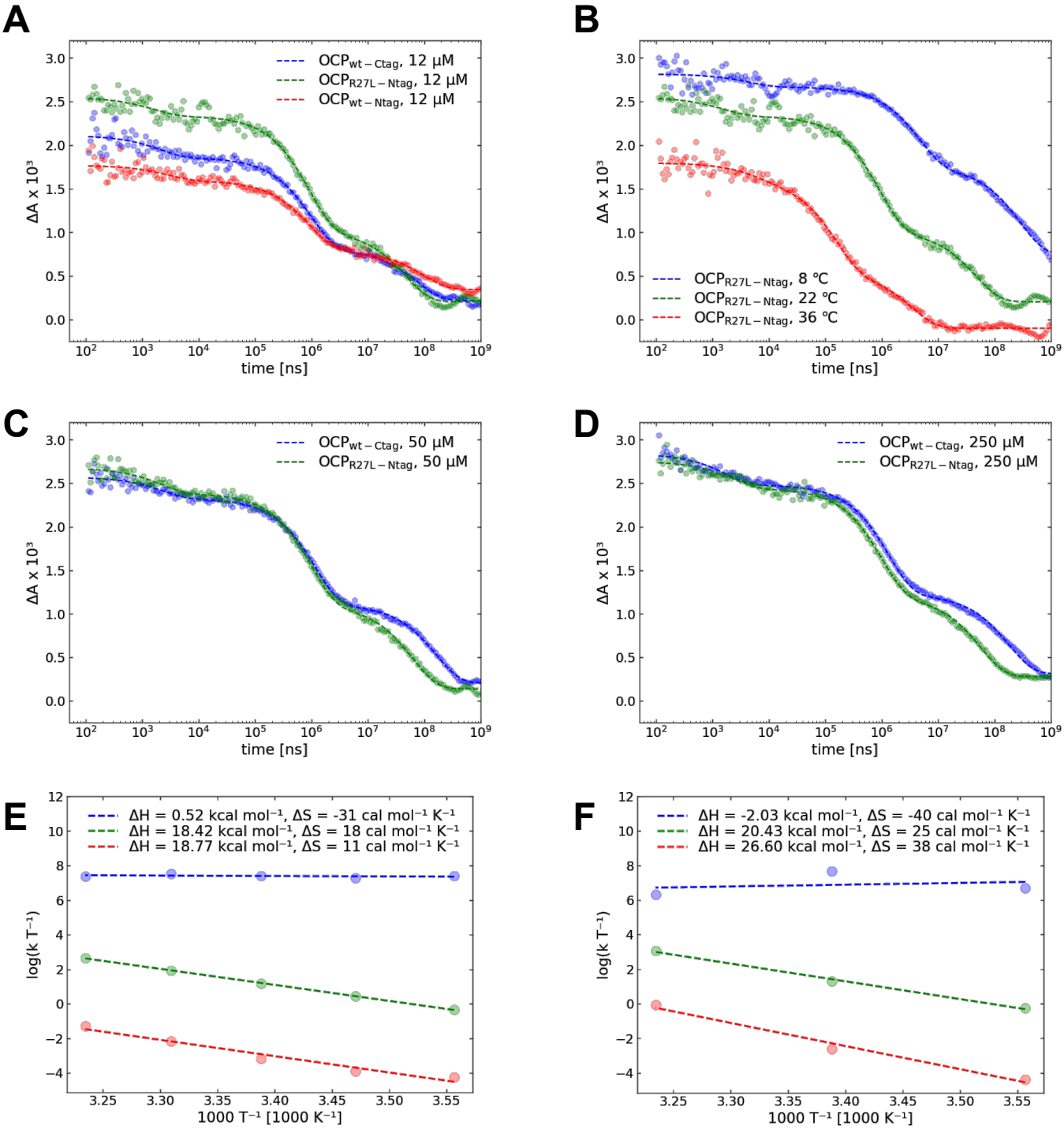

FIGURE 5. Transient absorption spectroscopy enables identification of three intermediate states on the 50 ns – 0.5 s time scale. The figure shows the time evolution of the difference absorption signal at 565 nm. (*A*) Nanosecond transient absorption data for $OCP_{wt\text{-}Ctag}$, $OCP_{wt\text{-}Ntag}$ and $OCP_{R27L\text{-}Ntag}$ at 12 μM. (*B*) Nanosecond transient absorption data for $OCP_{R27L\text{-}Ntag}$ at 12 μM and various temperatures. (*C* and *D*) Comparison of nanosecond transient absorption data between $OCP_{wt\text{-}Ctag}$ and $OCP_{R27L\text{-}Ntag}$ at 50 μM, and $OCP_{wt\text{-}Ctag}$ and $OCP_{R27L\text{-}Ntag}$ at 250 μM, respectively. (*E*-*F*) Eyring plots used to extract enthalpy and entropy of activation for $OCP_{wt\text{-}Ctag}$ (*E*) and $OCP_{R27L\text{-}Ntag}$ (*F*), (κ = 1 is assumed). See Figure S7 for complementary data.

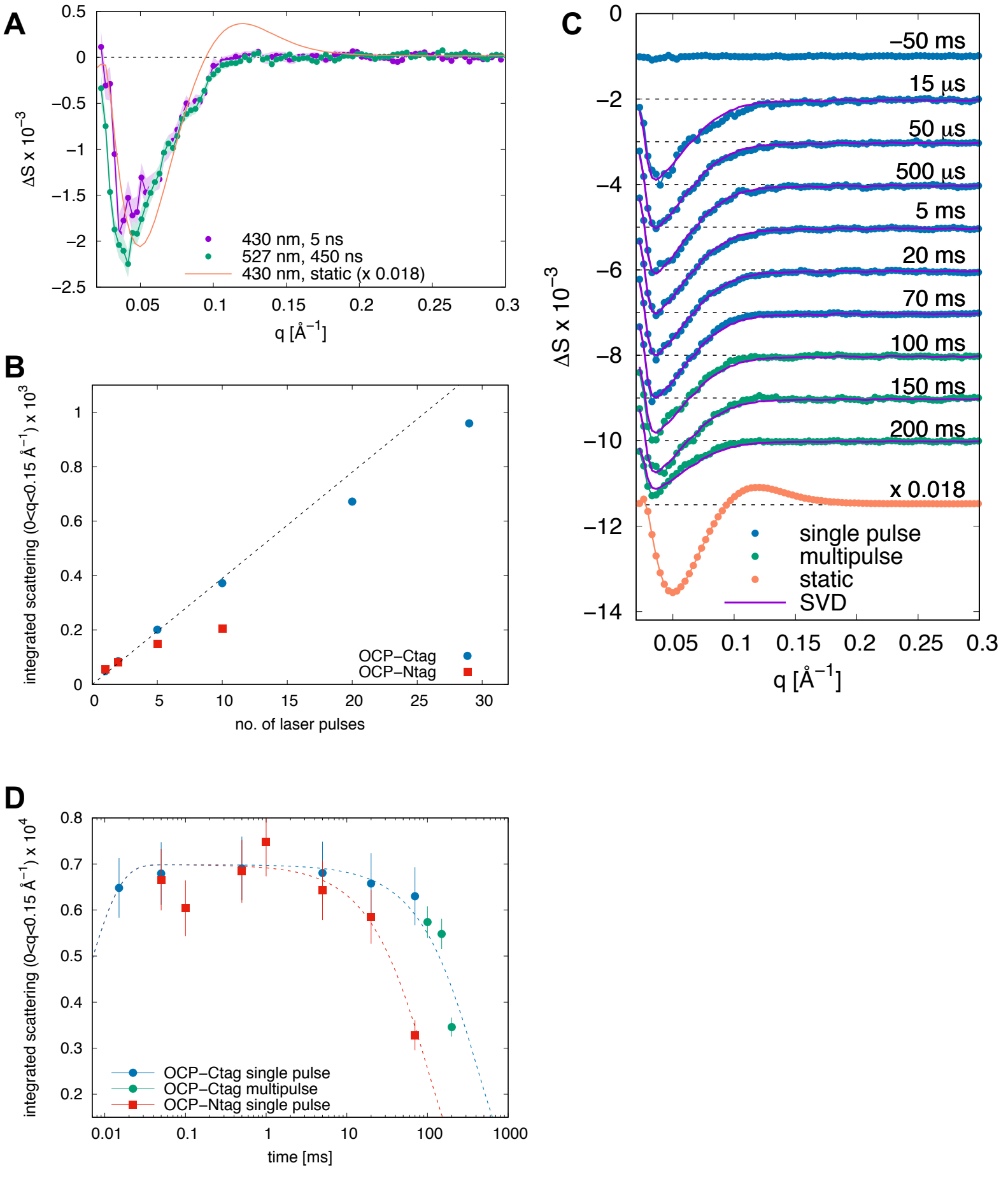

FIGURE 6. Time-resolved X-ray scattering reveals the kinetics of light-induced structural changes in the µs-ms time scale. (*A*) Comparison of the time resolved laser-on - laser-off X-ray difference pattern obtained 1 ms after excitation by either a 5 ns pulse at 430 nm or a 450 ns pulse at 527 nm. The static OCP^R - OCP^O X-ray difference pattern, calculated by subtracting the pattern of the dark-adapted sample from that of the continuously-illuminated sample (430 nm) and scaled by a factor 0.018, is shown for comparison. (*B*) Integrated difference scattering in the region 0 < q < 0.15 Å^{-1} as a function of the number of laser pulses (527 nm) for $OCP_{wt\text{-}Ctag}$ (blue circles) and $OCP_{wt\text{-}Ntag}$ (red squares). Pulse energy and duration were 2 mJ and 400 ns, respectively, and the pulses were spaced by 1 ms. (*C*) Light-induced time-resolved X-ray scattering difference patterns for $OCP_{wt\text{-}Ctag}$. The static OCP^R - OCP^O X-ray scattering difference pattern (scaled by a factor 0.018) is also shown for comparison. Data is vertically offset for clarity. (*D*) Time evolution of the integrated difference scattering in the region 0 < q < 0.15 Å^{-1} after laser excitation at 527 nm for $OCP_{wt\text{-}Ctag}$ (blue and green circles) and $OCP_{wt\text{-}Ntag}$ (red squares). Dashed lines are fitting curves with a double exponential function. Specific to the $OCP_{wt\text{-}Ctag}$ sample, the blue and green circles indicate patterns collected with either one or multiples pulses.

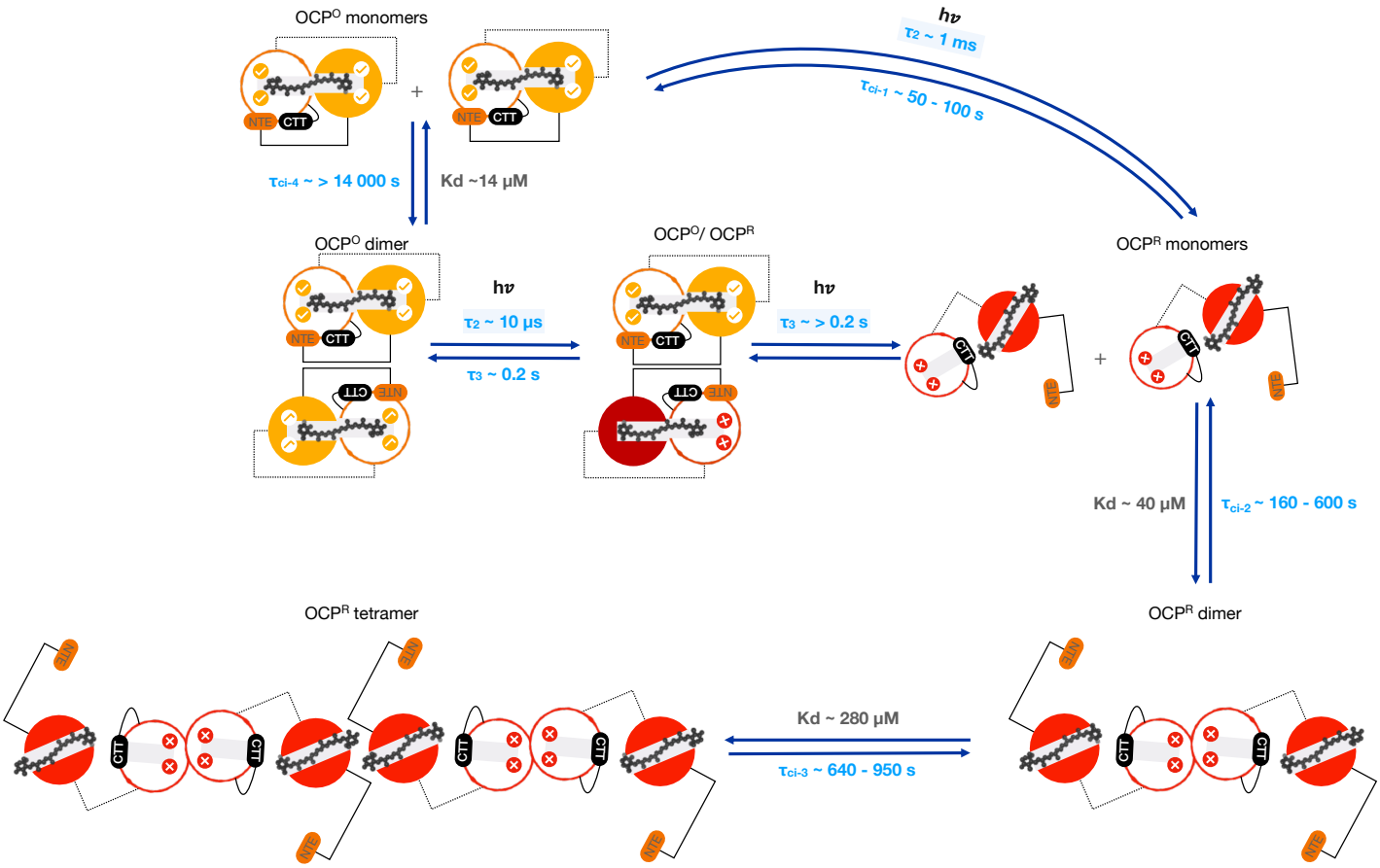

FIGURE 7. OCP photoactivation and recovery are limited by oligomerization processes. OCP monomers and dimers are represented schematically with their N-terminal (coloured in orange and red for OCP^O and OCP^R, respectively) and C-terminal domains (coloured in white) represented by two circles. The ground state keto-carotenoid is shown in grey. Ticks and crosses in the CTD respectively indicate presence and absence of H-bonds between the carotenoid and CTD residues Tyr201 and Trp288. The presence of ticks in the NTD indicate closure of the carotenoid tunnel at its NTD end and presence of π-stacking interactions between the carotenoid and NTD residues Tyr44 and Trp110. Our data show that dark-adapted OCP_{wt} forms dimers, with a dissociation constant of ~ 14 µM. The dimerization interface at play is likely that which has been repeatedly observed in the OCP crystal structures, since substitution for a leucine (L) of R27, involved in a conserved salt-bridge to D19 at this interface, fully abrogates dimerization. In the event where only one of the two monomers in a dimer is activated, it may undergo all photoactivation steps until formation of P_3, but will promptly revert to the dark state unless the second monomer is as well photoactivated (OCP^O/OCP^R). Indeed, domain dissociation may occur after dimer disassembly, which itself can only occur after NTE detachment, but the latter depends on the carotenoid achieving a successful transit across the NTD, *i.e.,* formation of P_3. In practice, this means that reaching the OCP^R state in a pulsed illumination experiment probing OCP_{wt} dimers is extremely unlikely unless re-excitation can be achieved within the lapse of the excitation pulse. Indeed, the probability that two monomers in a dimer can be activated by the same pulse is ~ $1e^{-5}$. Nonetheless, under continuous illumination, the OCP^R state can be accumulated, which first coalesces into dimers, with a dissociation constant similar to that displayed by dark-adapted OCP (~ 14 µM), but may as well form tetramers, with a nearly 20 times higher dissociation constant (~ 286 µM). Existence of these oligomers elevate the overall energy barrier for a full recovery of the starting dark OCP^O to occur, and therefore delay the upturn of the OCP^O state, as each OCP^R oligomer presents a different lifetime. It is yet the reassociation of dark monomers into dimers that constitute the limiting step in the recovery.

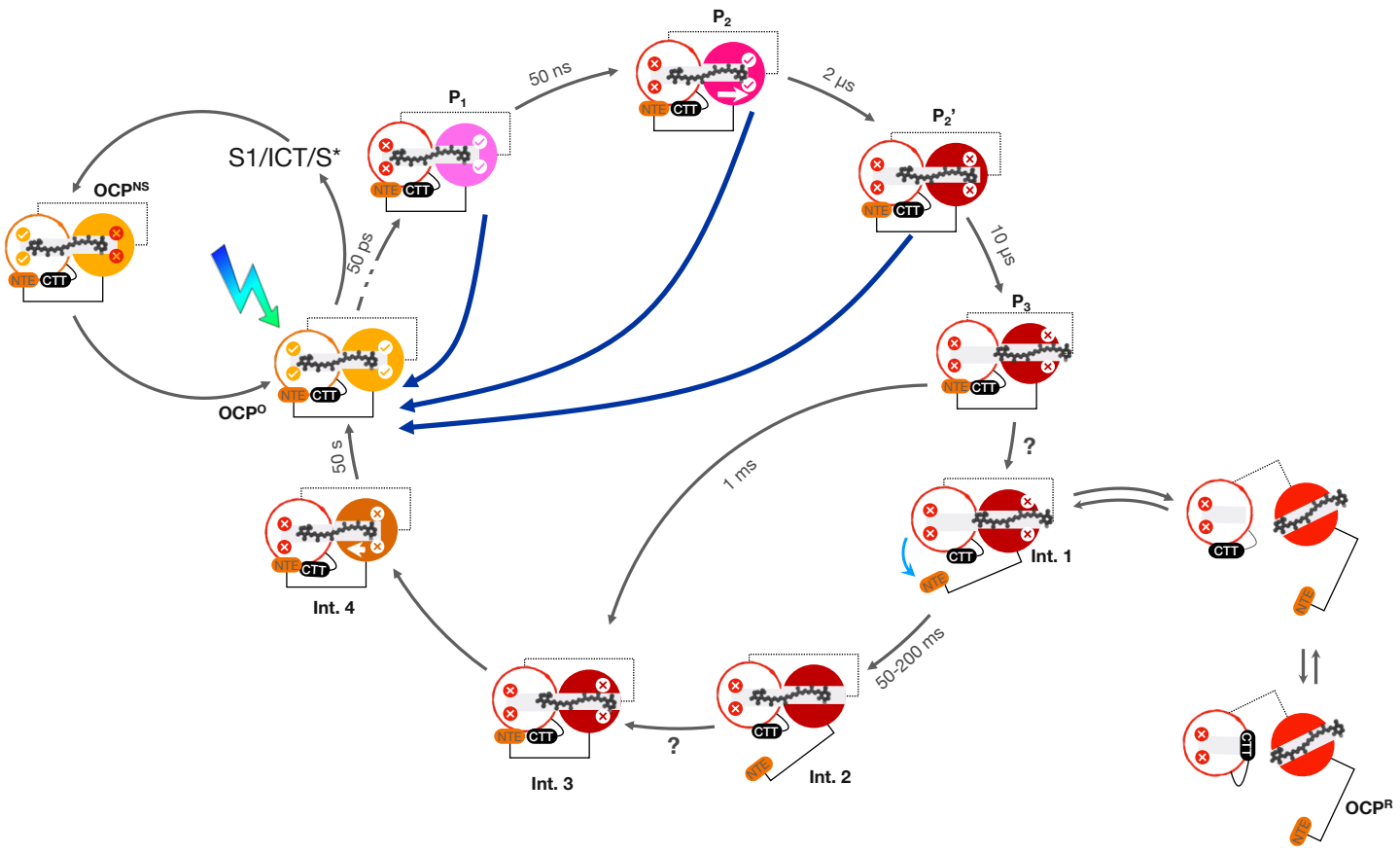

FIGURE 8. Proposed model for OCP photoactivation and recovery upon pulsed excitation. OCP is schematically represented with its N-terminal (coloured in orange for OCP^O, pink for P_1, magenta for P_2, red for P_2', P_3, OCP^R, Int.1, Int.2 and Int.3) and C-terminal domains (coloured in white), represented by two circles. The ground state keto-carotenoid is shown in grey. Ticks and crosses in the CTD respectively indicate presence and absence of H-bonds between the carotenoid and CTD residues Tyr201 and Trp288. Ticks and crosses in the NTD respectively indicate presence and absence of π-stacking interactions between the carotenoid and NTD residues Tyr44 and Trp110. For clarity, only the OCP monomer is shown. Complete migration of the carotenoid across the NTD tunnel requires the unsettling of these interactions and passage of a bottleneck contributed by NTD residues Leu37, Met83 and Met117, further down the tunnel. We posit that upon photoexcitation, the carotenoid of OCP forms multiple excited states, only one of which is parent to the first photoproduct P_1. Non-productive photoexcitation yet does not allow recovery of a photo-excitable state; instead, a numbed state forms that displays all spectral characteristics of the ground state but cannot be reactivated before a time delay estimated to lie between 0.5 µs and 1 ms. We can only presume that before then, important residues for the photoactivation mechanism (*e.g.* Y44 and W110) have not returned to their ground state positions, despite the carotenoid being at its H-bonding position and the protein therefore displaying an orange spectrum. Productive photoexcitation yields P_1, after rupture of H-bonds to the carotenoid; past 50 ns, the carotenoid repositions at the NTD/CTD interface (P_2), before bridging the above-mentioned bottleneck at 500 ns (P_2'). Conformational changes occur in the NTD domain, enabling the carotenoid to pass across the NTD wall and its β2 ionone ring to become solvent-exposed (P_3). At all steps before P_3, back-migration of the carotenoid to its dark-state position can occur with rapid recovery of the orange state, as the tunnel remains shielded from the bulk. After P_3, however, recovery follows another pathway that does not enable rapid recovery of the orange state spectrum. In the fraction of P_3 that does not recover, the NTE will eventually detach from the CTD β-sheet, however this step was not visible in our data. Either before or after detachment of the NTE, back-migration of the carotenoid can occur, with characteristic times of 1 and 50-200 ms, respectively. Separation of the two domains may yet take place before occurrence of carotenoid back-migration and NTE reattachment, yielding the minute-lived OCP^R state, after repositioning of the CTT over the empty CTD half of the carotenoid tunnel. P_3 could thus serve as an intermediate along the OCP^R to OCP^O recovery.

1315 **Supplementary Figures captions (599 words)**

1316 **FIGURE S1. Molecular envelopes and models fitted thereof for dark-adapted $OCP_{wt\text{-}Ctag}$ and**
1317 **$OCP_{R27L\text{-}Ntag}$ at the highest tested concentration.** The molecular envelopes determined based on
1318 static SAXS data are shown for (*A*) dark-adapted $OCP_{R27L\text{-}Ntag}$ and (*B*) $OCP_{wt\text{-}Ctag}$ at 14 and 23 mg/ml,
1319 respectively. Proposed models are overlaid on the molecular envelopes. For the dark-adapted
1320 $OCP_{R27L\text{-}Ntag}$, the molecular envelope is consistent with the presence of an OCP^{O} monomer, whereas
1321 for the dark-adapted $OCP_{wt\text{-}Ctag}$, it is better fitted by the crystallographic OCP^{O} dimer (pdb id: 3MG1).

1322 **FIGURE S2. Photoactivation of OCP at 30 mg/ml requires tens of minutes of illumination by a**
1323 **430 nm LED operating at 500 mW.** The figure shows X-ray scattering difference signals of $OCP_{wt\text{-}}$
1324 $_{Ctag}$ at 30 mg/ml in a 2 mm thick quartz capillary produced by continuous illumination with a 430 nm
1325 collimated LED source. The LED nominal power was first set at 250 mW, switched to 500 mW after
1326 ~750 s and kept on during 750 s after which saturation of the signal change was reached. Data was
1327 collected at the ID09 beamline (ESRF, Grenoble).

1328 **FIGURE S3. Structural recovery of $OCP^{O}_{wt\text{-}Ctag}$, following accumulation of $OCP^{R}_{wt\text{-}Ctag}$.** The plot
1329 shows the time evolution of the integrated intensity in the 0.05-0.5 $Å^{-1}$ region of the X-ray difference
1330 pattern $\Delta S = S(t) - S^{0}$, with S(t) and S^{0} the scattering patterns at a generic time t after switching off
1331 the 430 nm light and before the 430 nm irradiation procedure, respectively. The continuous line
1332 corresponds to a fit of the data by single exponential function.

1333 **FIGURE S4. The illumination procedure used to investigate OCP photoactivation and recovery**
1334 **does not damage the protein sample.** (*A*-*C*) Absorption spectra of OCP before (black) and after
1335 (green) 30 minutes illumination plus 16 hours of thermal recovery. (*A)* $OCP_{wt\text{-}Ntag}$ at 3 mg/ml, (*B*)
1336 $OCP_{R27L\text{-}Ntag}$ at 1.7 mg/ml and (*C*) $OCP_{wt\text{-}Ctag}$ at 1.7 mg/ml.

1337 **FIGURE S5. Global fitting of the recovery data for the different OCP variants.** (*A*, *B*) For each of
1338 the three OCP variants, thermal recovery was monitored at four concentrations and data were globally
1339 fitted using a model accounting either for three (*A*) or four (*B*) exponential components. The upper,
1340 middle and lower rows show fitting results for $OCP_{R27L\text{-}Ntag}$, $OCP_{wt\text{-}Ntag}$ and $OCP_{wt\text{-}Ctag}$, respectively.
1341 Fitting parameters are reported in Table S2 and S3.

1342 **FIGURE S6. Plots of the non-retained pre-exponential factors retrieved from fits of recovery**
1343 **data as a function of concentration.** (*A*) $OCP_{R27L\text{-}Ntag}$, (*B*) $OCP_{wt\text{-}Ntag}$ and (*C*) $OCP_{wt\text{-}Ctag}$. The
1344 $OCP_{R27L\text{-}Ntag}$ and $OCP_{wt\text{-}Ntag}$ data are best fit by a model accounting for three exponential components,
1345 whereas the $OCP_{wt\text{-}Ctag}$ data require inclusion of a fourth exponential component. Fitting parameters
1346 are reported in Table S2 and S3.

1347 **FIGURE S7. Nanosecond transient absorption kinetics for $OCP_{wt\ C\text{-}tag}$ at different temperatures.**
1348 (*A*-*E*) Difference absorption was monitored at both 440 and 565 nm, enabling to probe photoactivation
1349 and recovery at the two extremes of OCP^O and OCP^R absorption spectra, respectively. (*F*)
1350 Nanosecond transient absorption data for $OCP_{wt\ C\text{-}tag}$ at various temperatures, from 8 to 36 °C. See
1351 Table S4 for complementary data.

1352 **FIGURE S8. OCP dimerization increases the yields at shorter time delays and delays the**
1353 **occurrence of the last recovery step in the ns-s spectral evolution.** (*A*) Estimated yields of $OCP_{wt\text{-}}$
1354 $_{Ctag}$ red-states at various time delays and concentrations. The plot demonstrates that dimerization
1355 benefits the P_1 and P_3 yields. The OCP^R yield, however, only improves slightly. (*B*) The characteristic
1356 time for the third component used to fit the ns-s spectral evolution of $OCP_{wt\text{-}Ctag}$ increases as a function
1357 of OCP-dimer concentration. The average characteristic time extracted from fits of the $OCP_{R27L\text{-}Ntag}$
1358 data at various concentrations was used for zero dimer concentration.

1359

1360

1361 **Supplementary Tables:**

1362 TABLE S1. Data collection and structural information pertaining to static SAXS analysis on dark-
1363 adapted (OCP^O) and light-adapted (OCP^R) $OCP_{wt\text{-}Ctag}$ and $OCP_{R27L\text{-}Ntag}$.

1364 Table S2: Retained fitting parameters for the structural (SAXS) and spectroscopic (absorbance at 467
1365 nm) recovery of $OCP_{R27L\text{-}Ntag}$, $OCP_{wt\text{-}Ntag}$ and $OCP_{wt\text{-}Ctag}$, following accumulation of OCP^R by continuous
1366 illumination.

1367 Table S3: Non-retained fitting parameters for the spectral (absorbance at 467 nm) recovery of
1368 $OCP_{R27L\text{-}Ntag}$, $OCP_{wt\text{-}Ntag}$ and $OCP_{wt\text{-}Ctag}$, following accumulation of OCP^R by continuous illumination.

1369 TABLE S4. Fitted parameters extracted from nanosecond transient absorption data. Percentage
1370 contributions in the table are calculated as a given pre-exponential factor divided by $a_1 + a_2 + a_3 + a_4$.
1371 Measurements on $OCP_{wt\text{-}Ctag}$ at 22 °C were repeated twice to confirm repeatability (note replicated
1372 row in the table).

1373

1374

1375

1376